Ceramics-Silikáty 64 (3), 348-364 (2020)
www.ceramics-silikaty.cz doi: 10.13168/cs.2020.0023

EFFECT OF INTERFACE PROPERTIES ON THE NONLINEAR BEHAVIOUR OF LONG-FIBRE-REINFORCED UNIDIRECTIONAL CERAMIC-MATRIX MINI-COMPOSITES SUBJECTED TO TENSILE AND FATIGUE LOADING

#LONGBIAO LI*, ZHONGWEI ZHANG**, YUFENG LIU***

*College of Civil Aviation, Nanjing University of Aeronautics and Astronautics
No.29 Yudao St., Nanjing 210016, PR China
**Institute of Advanced Structure Technology, Beijing Institute of Technology, Beijing 100081, PR China
***Science and Technology of Advanced Functional Composite Materials Laboratory,
Aerospace Research Institute of Materials & Processing Technology, Beijing 100076, PR China

#E-mail: llb451@nuaa.edu.cn

Submitted January 15, 2020; accepted March 10, 2020

Keywords: Ceramic-matrix composites (CMCs), Mini, Matrix cracking, Interface debonding, Fibre failure, Hysteresis loops

In this paper, the effect of the interface properties between the fibre and the matrix on the nonlinear behaviour of long-fibre-reinforced unidirectional ceramic-matrix mini-composites (mini-CMCs) is investigated. The tensile nonlinear constitutive relationship and fatigue loading/unloading constitutive relationship are developed considering the different damage mechanisms of cracking in the matrix, debonding in the interface, and gradually the broken fibres. The relationships of the interface properties between the fibre and the matrix, the nonlinear tensile strain, and the fatigue loading/unloading hysteresis loops are established. The effects of the interface properties between the fibre and the matrix on the nonlinear tensile and fatigue loading/unloading damage evolution are analysed. The nonlinear tensile strain at the damage stage and the fracture strain of mini-CMCs decrease with the strong interface properties; and the fatigue loading/unloading hysteresis loops area and strain decrease, and the hysteresis modulus increases with the strong interface properties. The experimental tensile stress-strain curves and fatigue loading/unloading hysteresis loops of the Hi-Nicalon^{TM} and Tyranno^{TM} SiC/SiC mini-composites are predicted corresponding to the different interface properties.

INTRODUCTION

Ceramic-matrix composites (CMCs) are new types of thermal-structural-functional integrated materials with the advantages of metal materials, ceramic materials and carbon materials [1]. They have the characteristics of material-structural integration. Through the optimisation design of each structural unit, synergistic effects can be produced, and the high performance and reasonable matching of each performance can be achieved. Therefore, CMCs have high temperature resistance, corrosion resistance, wear resistance, a low density, a high specific strength and modulus, a low thermal expansion coefficient, insensitivity to cracks, no catastrophic damage and other advantages [2]. Since the 1990s, applications of CMCs have already been carried out in Europe and the United States on a demonstration and verification platform with thrust-to-weight ratios of 8-10 aeroengines (i.e., F119, EJ200, F414, M88-III, TRENT 800, etc.). The results show that fibre-reinforced CMCs can reduce the weight of stationary parts under moderate load by more than 50 %, and significantly improve their fatigue life. Generally speaking, intermediate-temperature and medium-load stationary parts such as a nozzle regulator/seal have already completed a life-cycle verification and entered the stage of practical application and batch production; high-temperature and medium-load stationary parts, such as a combustion chamber flame tube and an inner and outer lining are undergoing a life-cycle verification and are expected to enter the practical application stage; while high-temperature and high-load rotating parts such as a turbine rotor and turbine blade are still in the exploratory research stage [3, 4].

The composite materials interface refers to the area with significant changes in chemical composition between the matrix and the reinforcing phase. The interface properties between the fibre and the matrix play an important role on the mechanical behaviour of fibre-reinforced CMCs [5, 6]. The interphase transfers the load between the fibre and the matrix after interface debonding, protects the fibre against an oxidative environment, and deflects the matrix cracking along the interface for the nonlinear behaviour of the CMCs [7, 8, 9, 10, 11, 12, 13]. When the fibre/matrix interface is strongly bonded, the fibre cannot play the role of load carrying, and the fibre-reinforced CMC fractures become brittle; and when the fibre/matrix interface is weakly bonded, the energy dissipation mechanisms of the interface debonding and fibre pullout are not obvious, which limits the nonlinear behaviour of the CMC. When the interface bonding between the fibre and the matrix is suitable, the reinforcing fibre can transfer the load and debonding at a high applied stress, which deflects the matrix cracking and increases the energy dissipation. The tensile and fatigue loading/unloading behaviour is affected by the interface properties (i.e., interface shear stress and interface debonding energy) between the fibre and the matrix [14, 15, 16, 17, 18, 19, 20, 21]. Under tensile loading, the tensile stress-strain curves of fibre-reinforced CMCs can be divided into four different stages, i.e., (1) the linear-elastic stage, and the strain increases in direct proportion to the applied stress; (2) the damage stage with the matrix cracking and fibre debonding occurring at the interface, which makes the CMCs appear to have the characteristics of a pseudo-plastic fracture and high toughness [22]; (3) the damage stage with the saturation of the matrix cracking and the complete fibre debonding at the interface [23, 24]; and (4) gradually, the fibre fracture stage [25, 26]. The tensile properties including the elastic modulus, proportional limit stress, tensile strength, and fracture strain can be obtained through tensile tests, and used for the design of the CMC components [27]. Ahn et al. [28] investigated the interface deflection/penetration criterion at the fibre and the matrix interface using the energy release rate. Carrere et al. [29] investigated the matrix cracking deflection at the interphase of a mini-SiC/SiC composite with a Pyrocarbon (PyC) interphase. The deflection of the matrix cracking depends on the interface bond strength and interphase type. Sauder et al. [30] investigated the tensile and cyclic loading/unloading behaviour of a mini-SiC/SiC composite with a different interphase. The interphase thickness and the fibre surface roughness affect the tensile nonlinear and fracture strain of the mini-CMCs due to the different interface debonding conditions. Yu et al. [31] investigated the effect of the SiC coating thickness on the mechanical behaviour of a SiC/SiC composite. The flexural strength of a SiC/SiC composite initially increased with the SiC coating thickness and reached a peak value, and then decreased rapidly, however, the bending modulus increased with the SiC coating thickness. Kabel et al. [32] investigated the relationship between the the PyC interphase properties and the debonding shear strength of a SiC/SiC composite. Pryce and Smith [33] investigated the quasi-static tensile behaviour of a unidirectional and cross-ply SiC/CAS composite at room temperature and monitored the evolution of the matrix cracking. Based on the shear-lag model and experimental matrix cracking density, the tensile stress-strain curve of the unidirectional SiC/CAS composite was predicted [34]. Chateau et al. [35] investigated the damage evolution of a unidirectional SiC/SiC mini-composite using a 1D probabilistic model. The interfacial parameters are obtained by fitting the experimental characterisation. Morscher et al. [36] investigated the stress-dependent matrix cracking evolution of a 2D woven SiC/SiC composite, and the relationship for the stress-dependent matrix cracking could be related to the stress in the load-bearing CVI SiC matrix. Li et al. [37] developed a micromechanical model to predict the tensile behaviour of a unidirectional C/SiC composite, and established the relationship between the tensile curve and the internal damage mechanisms of the matrix cracking, interface debonding, and fibre failure. Li et al. [38] investigated the cyclic loading/unloading tensile behaviour of a unidirectional C/SiC composite at room temperature. The effect of the fibre failure on mechanical hysteresis loops was considered. Li [39, 40] investigated the cyclic loading/unloading hysteresis loops of a cross-ply SiC/MAS composite under the out-of-phase thermomechanical fatigue loading. The relationships between the phase angle, hysteresis loops, loading sequence, and environment temperature were established. The mini-composites (unidirectional composites containing a single bundle of fibres) were used to study the nonlinear behaviour of CMCs for different damage mechanisms [41, 42, 43]. The effect of the interface properties on the frictional heating [44, 45, 46], fatigue damage evolution [47, 48, 49, 50, 51, 52, 53, 54], and electrical resistance [55, 56] of unidirectional SiC/CAS, 2D SiC/SiC composites were investigated. The interface properties affect the tensile and fatigue behaviour of the fibre-reinforced CMCs, especially the nonlinear tensile behaviour and the mechanical hysteresis loops. It is necessary to perform the investigations on the effect of the interface properties on the tensile and fatigue behaviour of the fibre-reinforced CMCs, in order to establish the relationships between the interface properties and the mechanical behaviour of the CMCs.

In this paper, the nonlinear behaviour of mini-CMCs for different interface properties subjected to tensile and fatigue loading/unloading is investigated. The nonlinear constitutive models for the tensile and fatigue loading/unloading hysteresis loops are developed considering the different damage mechanisms and interface properties. The effect of the interface properties on the nonlinear strain and fracture strain under tensile loading, fatigue loading/unloading hysteresis loops area, strain, and modulus is discussed. The experimental tensile strain and fatigue loading/unloading hysteresis loops of the Hi-Nicalon^{TM} and Tyranno^{TM} SiC/SiC mini-composites with different interphase properties are predicted.

EXPERIMENTAL

The Hi-Nicalon^{TM} S (Nippon Carbon Co. Ltd., Takauchi, Japan) and Tyranno SA3 (UBE Industries, Tokyo, Japan) tows reinforced SiC matrix (SiC/SiC) mini-composites were fabricated using the chemical vapour infiltration (CVI) method. The SiC tows were coated with a single layer of pyrocarbon (PyC) with a thickness of 30 or 150 nm, and a multilayer of PyC and SiC with a thickness of 150 nm. The tensile and cyclic loading/unloading experimental results were performed and obtained per Sauder et al. [30]. The tensile and cyclic loading/unloading tests were performed at room temperature at a constant strain rate of 50 μm min^{-1}. The deformations of the mini-composite were measured using two-parallel linear-variable differential transformer extensometers.

THEORETICAL

In the present analysis, the constitutive models for the tensile and fatigue loading/unloading of the mini-CMCs have been developed considering the multiple damage mechanisms and interface properties. The stochastic matrix cracking model, fracture mechanics approach, and Global Load Sharing (GLS) criterion are used to determine the space between the matrix cracking, fibre debonding length, fibre failure probability and intact fibre stress, respectively. Under fatigue loading/unloading, the repeated sliding at the interface is taken into consideration for the mechanical hysteresis loops.

Tensile constitutive model

Under tensile loading, the nonlinear aspect of the CMCs is caused by the different damage mechanisms. In order to establish the nonlinear tensile constitutive model of the CMCs, the micro stress field of the fibre, matrix and the interface along the fibre direction for the multiple damage status should be analysed. When damage occurs, a unit cell is extracted from the mini-CMCs, as shown in Figure 1. The shear-lag model can be used to analyse the micro stress field of the damaged composite [57]. The fibre axial stress distribution can be determined using Equation 1 for the different damage regions [37].

$$\sigma_{\mathrm{f}}(x)=\begin{cases}\Phi-\dfrac{2\tau_{\mathrm{i}}}{r_{\mathrm{f}}}x,\ x\in[0,\ l_{\mathrm{d}}]\\ \sigma_{\mathrm{fo}}+\left(\Phi-\sigma_{\mathrm{fo}}-2\dfrac{l_{\mathrm{d}}}{r_{\mathrm{f}}}\tau_{\mathrm{i}}\right)\exp\left(-\rho\dfrac{x-l_{\mathrm{d}}}{r_{\mathrm{f}}}\right),\\ x\in[l_{\mathrm{d}},\ l_{\mathrm{c}}/2]\end{cases} \quad (1)$$

where r_f denotes the fibre radius; l_{d} denotes the interface debonding length and can be determined using the fracture mechanics approach [37]; l_{c} denotes the matrix crack spacing and can be determined using the stochastic matrix cracking model [37]; σ_{fo} denotes the fibre axial stress in the interface bonding region; ρ denotes the shear-lag model parameter; τ_{i} denotes the interface shear stress; and Φ denotes the intact fibre stress.

$$l_{\mathrm{d}}=\frac{r_{\mathrm{f}}}{2}\left(\frac{V_{\mathrm{m}}E_{\mathrm{m}}\sigma}{V_{\mathrm{f}}E_{\mathrm{c}}\tau_{\mathrm{i}}}-\frac{1}{\rho}\right)-\sqrt{\left(\frac{r_{\mathrm{f}}}{2\rho}\right)^2+\frac{r_{\mathrm{f}}V_{\mathrm{m}}E_{\mathrm{m}}E_{\mathrm{f}}}{E_{\mathrm{c}}\tau_{\mathrm{i}}^2}\zeta_{\mathrm{d}}} \quad (2)$$

$$l_{\mathrm{c}}=l_{\mathrm{sat}}\left\{1-\exp\left[-\left(\frac{\sigma_{\mathrm{m}}}{\sigma_{\mathrm{R}}}\right)^m\right]\right\}^{-1} \quad (3)$$

where V_{m} denotes the matrix volume; E_{m} denotes the matrix elastic modulus; E_{c} denotes the composite elastic modulus; ζ_{d} denotes the interface debonding energy; l_{sat} denotes the saturation matrix crack spacing; σ_{m} denotes the matrix stress; σ_{R} denotes the matrix cracking characteristic stress; and m denotes the matrix Weibull modulus.

Considering multiple damage mechanisms, the nonlinear constitutive relationship of the mini-CMCs can be determined using the following equation [37]:

$$\begin{aligned}\varepsilon_{\mathrm{c}}=&\frac{\Phi}{E_{\mathrm{f}}}\frac{2l_{\mathrm{d}}}{l_{\mathrm{c}}}-\frac{\tau_{\mathrm{i}}}{E_{\mathrm{f}}}\frac{2l_{\mathrm{d}}^2}{r_{\mathrm{f}}l_{\mathrm{c}}}+\frac{2\sigma_{\mathrm{fo}}}{E_{\mathrm{f}}l_{\mathrm{c}}}\left(\frac{l_{\mathrm{c}}}{2}-l_{\mathrm{d}}\right)-\\&-\frac{1}{\rho E_{\mathrm{f}}}\frac{2r_{\mathrm{f}}}{l_{\mathrm{c}}}\left(\Phi-\sigma_{\mathrm{fo}}-2\frac{l_{\mathrm{d}}}{r_{\mathrm{f}}}\tau_{\mathrm{i}}\right)\times\\&\times\left[\exp\left(-\rho\frac{l_{\mathrm{c}}/2-l_{\mathrm{d}}}{r_{\mathrm{f}}}\right)-1\right]-(\alpha_{\mathrm{c}}-\alpha_{\mathrm{f}})\Delta\mathrm{T}\end{aligned} \quad (4)$$

where α_f and α_c denote the fibre and the composite thermal expansion coefficient, respectively; and ΔT denotes the temperature difference between the testing and fabricated temperature.

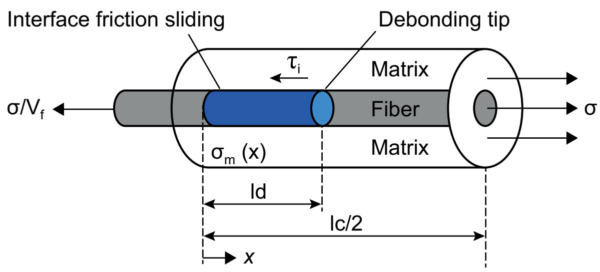

Figure 1. The unit cell of the shear-lag model.

Fatigue loading/unloading constitutive model

Under fatigue loading/unloading, the interface damage status affects the mechanical hysteresis loops. The fatigue loading/unloading constitutive model can be divided into two cases, i.e., (1) the partial debonding at the fibre interface; and, (2) the complete debonding at the fibre interface.

For the partial debonding at the fibre interface, the fatigue loading/unloading constitutive relationship can be determined using the following equations. [38]

$$\begin{aligned}\varepsilon_{\mathrm{unloading}}=&\frac{\Phi_U}{E_{\mathrm{f}}}+4\frac{\tau_{\mathrm{i}}}{E_{\mathrm{f}}}\frac{y^2}{r_{\mathrm{f}}l_{\mathrm{c}}}-\frac{\tau_{\mathrm{i}}}{E_{\mathrm{f}}}\frac{(2y-l_{\mathrm{d}})(2y+l_{\mathrm{d}}-l_{\mathrm{c}})}{r_{\mathrm{f}}l_{\mathrm{c}}}-\\&-(\alpha_{\mathrm{c}}-\alpha_{\mathrm{f}})\Delta\mathrm{T}\end{aligned} \quad (5)$$

$$\varepsilon_{\text{reloading}} = \frac{\Phi_R}{E_f} - 4\frac{\tau_i}{E_f}\frac{z^2}{r_f l_c} + 4\frac{\tau_i}{E_f}\frac{(y-2z)^2}{r_f l_c} + 2\frac{\tau_i}{E_f}\frac{(l_d - 2y + 2z)(l_d + 2y - 2z - l_c)}{r_f l_c} - (\alpha_c - \alpha_f)\Delta T \qquad (6)$$

where $\varepsilon_{unloading}$ denotes the unloading strain; and $\varepsilon_{reloading}$ denotes the reloading strain; Φ_U and Φ_R denote the intact fibres stress upon unloading and reloading, respectively; and y and z denote the interface counter-slip length and new-slip length, respectively.

For the complete debonding at the fibre interface, the fatigue loading/unloading constitutive relationship can be determined using the following equations [38]:

$$\varepsilon_{\text{unloading}} = \frac{\Phi_U}{E_f} + 4\frac{\tau_i}{E_f}\frac{y^2}{r_f l_c} - 2\frac{\tau_i}{E_f}\frac{(2y - l_c/2)^2}{r_f l_c} - (\alpha_c - \alpha_f)\Delta T \qquad (7)$$

$$\varepsilon_{\text{reloading}} = \frac{\Phi_R}{E_f} - 4\frac{\tau_i}{E_f}\frac{z^2}{r_f l_c} + 4\frac{\tau_i}{E_f}\frac{(y-2z)^2}{r_f l_c} - 2\frac{\tau_i}{E_f}\frac{(l_c/2 - 2y + 2z)^2}{r_f l_c} - (\alpha_c - \alpha_f)\Delta T \qquad (8)$$

RESULTS AND DISCUSSION

The interface properties affect the nonlinear mechanical behaviour of the CMCs, especially subjected to the tensile and fatigue loading/unloading conditions. For the CMCs, the interface properties can be characterised using two parameters of the interface shear stress and the interface debonding energy. In this section, the effects of the interface properties on the nonlinear behaviour of the mini-CMCs subjected to the tensile and fatigue loading/unloading are analysed. The Hi-Nicalon™ Type S SiC/SiC mini-composite was used for the case analysis, and the material properties are given by [30]: $V_f = 44$ %, $E_f = 372$ GPa, $E_m = 550$ GPa, $r_f = 6.5$ µm, $\alpha_f = 4.5 \times 10^{-6}$/°C, $\alpha_m = 4.6 \times 10^{-6}$/°C, $\Delta T = -1000$ °C, $\zeta_d = 0.1$ J·m^{-2}, $\tau_i = 20$ MPa.

Effect of the interface properties on tensile nonlinear strain

Li and Song [59] developed an approach to estimate the interface shear stress of fibre-reinforced CMCs using hysteresis loops. The range of the interface shear stress of a unidirectional SiC/CAS composite is between τ_i =10 and 30 MPa. The effect of the interface shear stress (i.e., τ_i = 10, 20, and 30 MPa) on the tensile nonlinear strain and the interface debonding of the SiC/SiC mini-composite is shown in Figure 2. When the interface shear stress increases from τ_i = 10 MPa to τ_i = 30 MPa, the composite strain corresponding to the different damage stages of matrix cracking, interface debonding, and fibre failure decreases, and the composite failure strain decreases, due to the decrease in the interface debonding length. When the interface shear stress increases, the stress transfer between the fibre and the matrix increases, and the resistance to the interface debonding also increases, leading to a decrease in the interface debonding length and the nonlinear tensile strain [58]. The composite failure strain decreases from ε_f = 0.58 % at τ_i = 10 MPa to ε_f = 0.47 % at τ_i = 30 MPa. The interface complete debonding stress increases with the interface shear stress. The interface complete stress increases from σ = 660 MPa at τ_i = 10 MPa to σ = 737 MPa at τ_i = 20 MPa.

Vagaggini et al. [60] investigated the constituent properties of fibre-reinforced CMCs using hysteresis loops. It was found that the value of the interface debonding energy is ζ_d = 0 ~ 5 J·m^{-2}. The effect of the interface debonding energy (i.e., ζ_d = 1, 2, and 3 J·m^{-2})

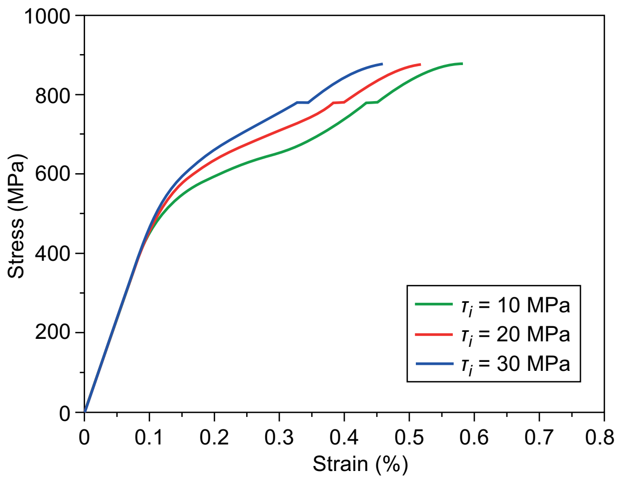

a)

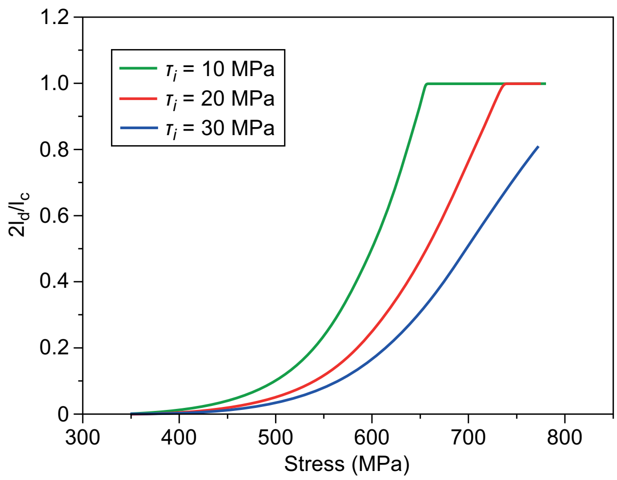

b)

Figure 2. The effect of the interface shear stress on: a) the tensile stress-strain curves; b) the interface debonding length versus the applied stress curves of the Hi-NicalonTM Type S SiC/SiC mini-composite.

on the tensile nonlinear strain and the interface debonding of the SiC/SiC mini-composite is shown in Figure 3. When the interface debonding energy increases from ζ_d = 1 J·m^{-2} to ζ_d = 3 J·m^{-2}, the composite strain corresponding to the different damage stages decreases, and the composite failure strain decreases, due to the decrease in the interface debonding length. When the interface debonding energy increases, the energy needed for the interface debonding increases, leading to a decrease in the interface debonding length, and a decrease in the nonlinear strain. The composite failure strain decreases from ε_f = 0.53 % at ζ_d = 1 J·m^{-2} to ε_f = 0.4 % at ζ_d = = 3 J·m^{-2}. At the same applied stress of σ = 780, the interface debonding length decreases from $2l_d/l_c$ = 1.0 at ζ_d = 1 J·m^{-2} to $2l_d/l_c$ = 0.38 at ζ_d = 3 J·m^{-2}.

Effect of the interface properties on the fatigue loading/unloading hysteresis loops

The effect of the interface shear stress (i.e., τ_i = 10, 20, and 30 MPa) on the fatigue loading/unloading hysteresis loops and the interface slip of the SiC/SiC mini-composite under the peak stress of σ_{max} = 500 MPa is shown in Figure 4. When the interface shear stress increases from τ_i = 10 MPa to τ_i = 30 MPa, the fatigue loading/unloading hysteresis loops area, peak and valley strain decrease, and the fatigue loading/unloading hysteresis modulus increases, due to the decrease in the interface slip length. When the interface shear stress increases, the resistance to the interface debonding increases, leading to a decrease in the interface debonding

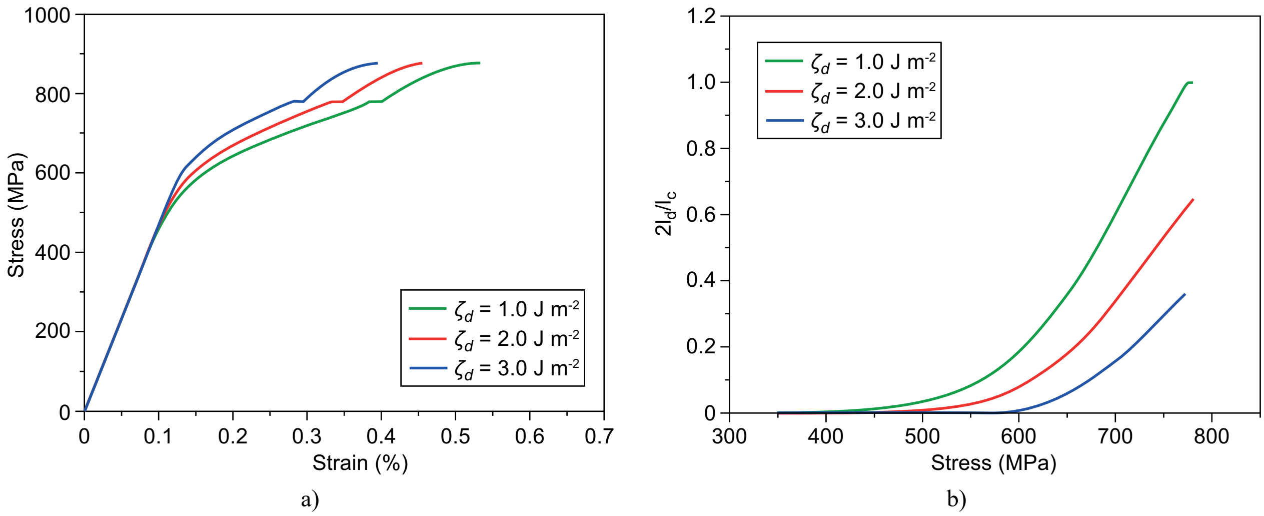

Figure 3. The effect of the interface debonding energy on: a) the tensile stress-strain curves; b) the interface debonding length versus the applied stress curves of the Hi-NicalonTM Type S SiC/SiC mini-composite.

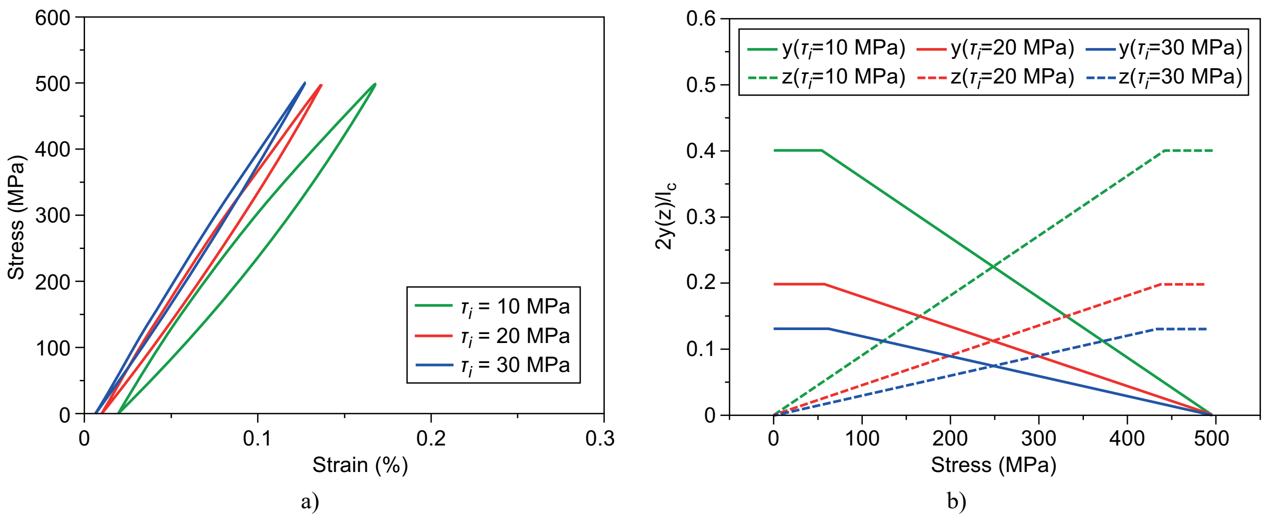

Figure 4. The effect of the interface shear stress on: a) the fatigue loading/unloading hysteresis loops; b) the interface slip lengths versus the applied stress curves of the Hi-NicalonTM Type S SiC/SiC mini-composite.

and slip length, and a decrease in the area, peak and valley strain of the fatigue loading/unloading hysteresis loops. Under the peak stress of σ_{max} = 500 MPa, the interface slip range decreases from 40 % of the matrix crack spacing at τ_i = 10 MPa to 13 % of the matrix crack spacing at τ_i = 30 MPa.

The effect of the interface debonding energy (i.e., ζ_d = 1, 3, and 5 J·m^{-2}) on the fatigue loading/unloading hysteresis loops and the interface slip of the SiC/SiC mini-composite under the peak stress of σ_{max} = 800 MPa is shown in Figure 5. When the interface debonding energy increases from ζ_d = 1 J·m^{-2} to ζ_d = 5 J·m^{-2}, the fatigue loading/unloading hysteresis loops area, peak and valley strain decrease, and the fatigue hysteresis modulus increases, due to the decrease in the interface slip length. When the interface debonding energy increases, the energy needed for the interface debonding increases, leading to a decrease in the interface debonding length, and a decrease in the area, peak and valley strain of the fatigue loading/unloading hysteresis loops. Under the peak stress of σ_{max} = 800 MPa, the interface slip range decreases from 38 % of the matrix crack spacing at ζ_d = 1 J·m^{-2} to 20 % of the matrix crack spacing at ζ_d = 5 J·m^{-2}.

EXPERIMENTAL

Sauder et al. [30] performed investigations on the effect of the tensile and cyclic loading/unloading tensile behaviour of SiC/SiC mini-composites with different interface properties. The material properties of the Hi-Nicalon^{TM} and Tyranno^{TM} SiC/SiC mini-composites are listed in Table 1. The tensile nonlinear strain, matrix cracking evolution, fatigue loading/unloading hysteresis loops, and the interface debonding and slip of Hi-Nicalon^{TM} and Tyranno^{TM} SiC/SiC minicomposites are predicted considering the different interface properties.

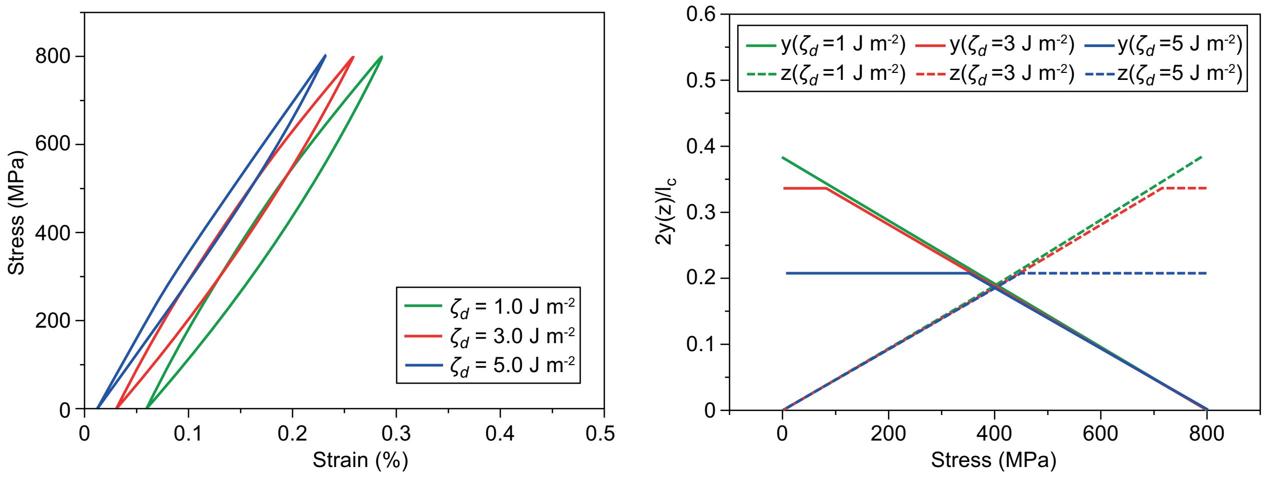

Figure 5. The effect of the interface debonding energy on: a) the fatigue loading/unloading hysteresis loops; d) the interface slip lengths versus the applied stress curves of the Hi-NicalonTM Type S SiC/SiC mini-composite.

Table 1. The material properties of the unidirectional SiC/SiC mini-composites.

Items	Type A Hi-Nicalon^{TM} S SiC/SiC	Type B Hi-Nicalon^{TM} S SiC/SiC	Type C Hi-Nicalon^{TM} S SiC/SiC	Tyranno^{TM} SA3 SiC/SiC
Interphase	PyC (150 nm)	PyC/SiC/PyC/SiC/PyC (150 nm)	PyC (30 nm)	PyC (150 nm)
r_f (μm)	6.5	6.5	6.5	3.5
V_f (%)	46	44	40	43
E_f (GPa)	372	372	372	387
E_m (GPa)	400	550	550	400
α_f (10^{-6}/°C)	3.5	4.5	4.5	4
α_m (10^{-6}/°C)	4.6	4.6	4.6	4.6
τ_i (MPa)	9	20	10	100
ζ_d (J·m^{-2})	0.1	0.3	0.1	0.1
σ_{UTS} (MPa)	940	878	860	1116

Tensile nonlinear strain and fatigue loading/unloading hysteresis loops of the Type A Hi-Nicalon™ Type S SiC/SiC mini-composite

The experimental and predicted tensile nonlinear strain, matrix cracking evolution, fatigue loading/unloading hysteresis loops, and interface debonding and sliding of the Type A Hi-Nicalon™ Type S SiC/SiC mini-composite are shown in Figures 6-9 and Table 2.

Under tensile loading, the tensile stress-strain curve of the SiC/SiC mini-composite is predicted using the tensile constitutive model of Equation 4, which exhibits obvious nonlinear behaviour between the first matrix cracking stress of about $\sigma_{mc} = 400$ MPa and the saturation matrix cracking stress of about $\sigma_{sat} = 800$ MPa, and the composite tensile strength is about $\sigma_{UTS} = 940$ MPa with the failure strain of $\varepsilon_f = 0.64$ %, as shown in Figure 6a.

Table 2. The tensile nonlinear strain and fatigue loading/unloading hysteresis loops of the Type A Hi-NicalonTM Type S SiC/SiC mini-composite.

Tensile						
Items	σ_{mc} (MPa)	σ_{sat} (MPa)	σ_{UTS} (MPa)	ε_f (%)	λ_{mc} (mm^{-1})	λ_{sat} (mm^{-1})
Value	400	800	940	0.64	0.24	2.85

Fatigue					
Items	σ_{max} (MPa)	$2l_d/l_c$	$y(z)/l_d$	σ_{tr_fu} (MPa)	σ_{tr_fr} (MPa)
Value	500	0.56	0.86	–	–
	800	1.0	1.0	400	400
	850	1.0	1.0	467.5	382.5

The matrix cracking density is predicted using Equation 3 and increases from $\lambda_{mc} = 0.24$/mm at $\sigma_{mc} = 400$ MPa to the saturation matrix cracking density of $\lambda_{sat} = 2.85$ mm^{-1} at $\sigma_{sat} = 800$ MPa, as shown in Figure 6b.

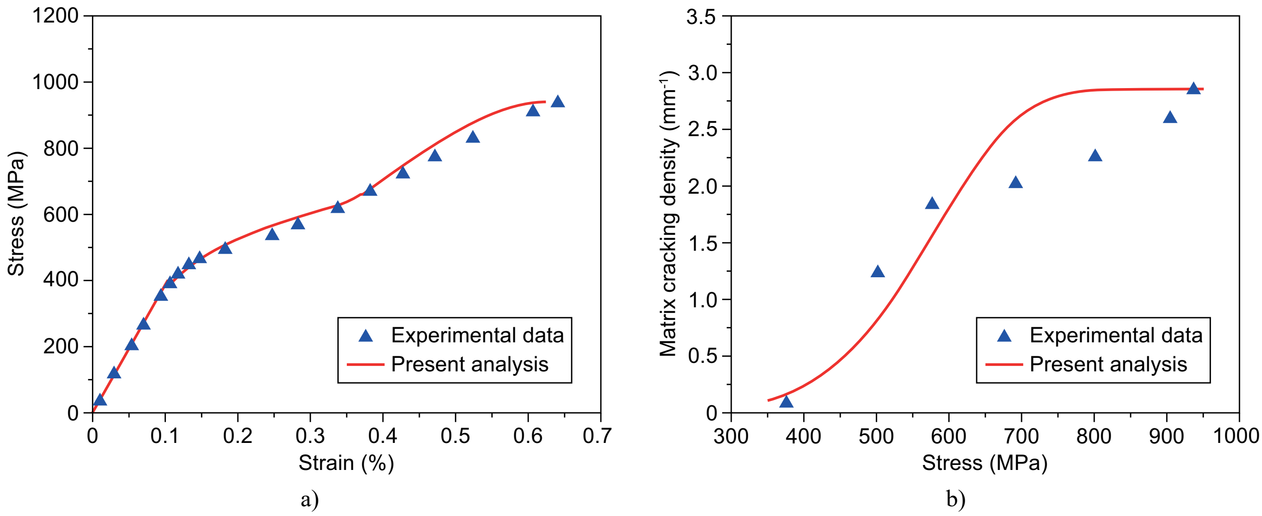

Figure 6. The experimental and predicted tensile stress-strain curves (a) and the experimental and predicted matrix cracking den-sity versus the applied stress curves of the Type A Hi-NicalonTM Type S SiC/SiC mini-composite (b).

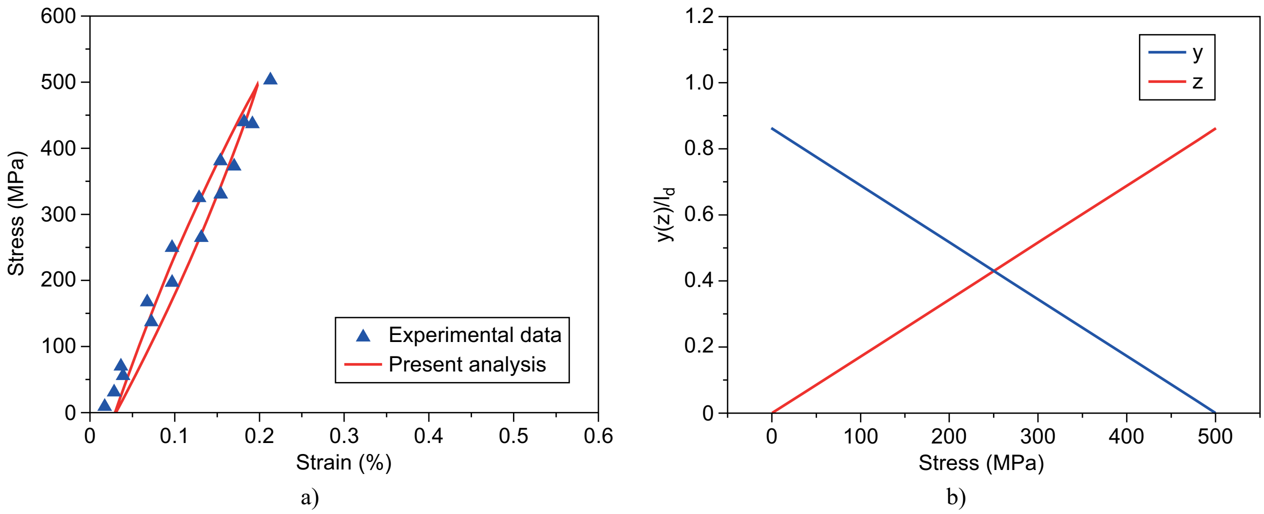

Figure 7. The experimental and predicted fatigue loading/unloading hysteresis loops(a) and the experimental and predicted inter-face slip length versus the applied stress curves of the Type A Hi-NicalonTM Type S SiC/SiC mini-composite under the peak stress of $\sigma_{max} = 500$ MPa (b).

Under fatigue loading/unloading, the interface partially debonds (i.e., $2l_d/l_c = 0.56$), and the fibre partially slides relative to the matrix in the interface debonding region (i.e., $y(z)/l_d = 0.86$) under the peak stress of $\sigma_{max} = 500$ MPa, and the interface debonding length is determined using Equation 2, and the fatigue loading/unloading hysteresis loop is predicted by Equations 5 and 6, as shown in Figure 7; and under the peak stress of $\sigma_{max} = 800$, and 850 MPa, the fibre/matrix interface completely debonds (i.e., $2l_d/l_c = 1$), and the fibre completely slides relative to the matrix at the matrix crack spacing (i.e., $y(z)/l_d = 1$), and the interface debonding length is determined using Equation 2, and the fatigue loading/unloading hysteresis loop is predicted by Equations 7 and 8, as shown in Figures 8 and 9.

Table 3. The tensile nonlinear strain and fatigue loading/unloading hysteresis loops of the Type B Hi-NicalonTM Type S SiC/SiC mini-composite.

Tensile						
Items	σ_{mc} (MPa)	σ_{sat} (MPa)	σ_{UTS} (MPa)	ε_f (%)	λ_{mc} (mm^{-1})	λ_{sat} (mm^{-1})
Value	350	780	878	0.54	1.1	4.5

Fatigue					
Items	σ_{max} (MPa)	$2l_d/l_c$	$y(z)/l_d$	σ_{tr_fu} (MPa)	σ_{tr_fr} (MPa)
Value	632	0.32	0.88	–	–
	699	0.6	0.84	–	–
	724	1.0	0.55	–	–
	778	1.0	0.79	–	–
	837	1.0	1.0	41.8	795.2
	878	1.0	1.0	175.6	702.4

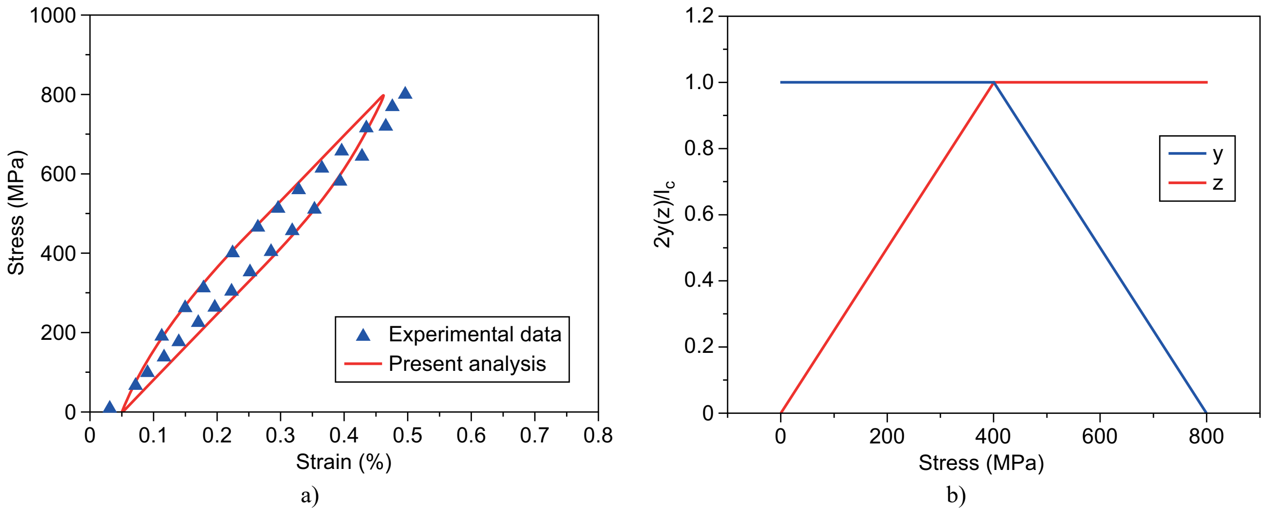

Figure 8. The experimental and predicted fatigue loading/unloading hysteresis loops (a) and the experimental and predicted inter-face slip length versus the applied stress curves of the Type A Hi-NicalonTM Type S SiC/SiC mini-composite under the peak stress of $\sigma_{max} = 800$ MPa (b).

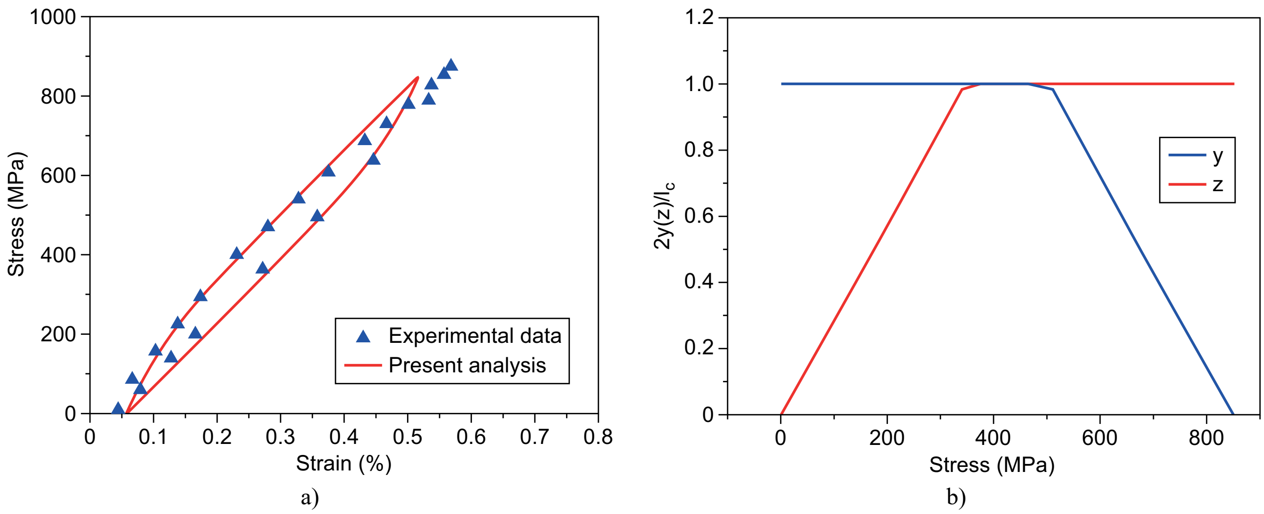

Figure 9. The experimental and predicted fatigue loading/unloading hysteresis loops (a) and the experimental and predicted inter-face slip lengths versus the applied stress curves of the Type A Hi-NicalonTM Type S SiC/SiC mini-composite under the peak stress of $\sigma_{max} = 850$ MPa (b).

Tensile nonlinear strain and fatigue loading/unloading hysteresis loops of the Type B Hi-Nicalon™ Type S SiC/SiC mini-composite

For the Type B Hi-Nicalon™ Type S SiC/SiC mini-composite, the experimental and predicted tensile nonlinear strain, and matrix cracking evolution are shown in Figure 10 and Table 3. The tensile stress-strain curve is predicted using the tensile constitutive model of Equation 4, which exhibits obvious nonlinear behaviour between the first matrix cracking stress of σ_{mc} = 350 MPa and the saturation matrix cracking stress of σ_{sat} = 780 MPa, and the composite tensile strength is about σ_{UTS} = 878 MPa with the failure strain of ε_f = 0.54 %. The matrix cracking density is predicted using Equation 3 and increases from λ_{mc} = 1.1 mm^{-1} at σ_{mc} = 600 MPa to λ_{sat} = 4.5 mm^{-1} at σ_{sat} = 875 MPa.

The experimental and predicted fatigue loading/unloading hysteresis loops and interface slip under the peak stresses of σ_{max} = 632, 669, 724, 778, 837, and 878 MPa are shown in Figures 11-16 and Table 3. Upon unloading and reloading, the interface partially debonds and the fibre partially slides relative to the matrix under the peak stresses of σ_{max} = 632 and 669 MPa, and the interface debonding length is determined using Equation 2, and the fatigue loading/unloading hysteresis loop is predicted by Equations 5 and 6; the interface completely debonds and the fibre partially slides relative to the matrix under the peak stresses of σ_{max} = 724 and 778 MPa, and the interface debonding length is determined using Equation 2, and the fatigue loading/unloading hysteresis loop is predicted by Equations 7 and 8; and the interface completely debonds and the fibre completely slides relative to the matrix under the peak stresses of σ_{max} = = 837 and 878 MPa, and the interface debonding length

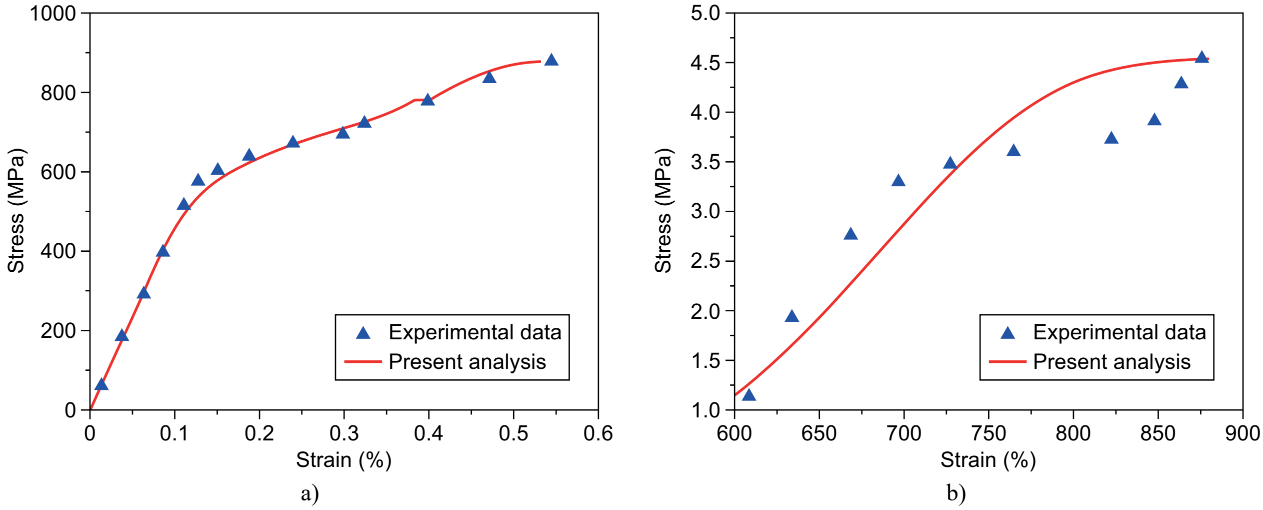

Figure 10. The experimental and predicted tensile stress-strain curves (a) and the experimental and predicted matrix cracking density versus the applied stress curves of the Type B Hi-NicalonTM Type S SiC/SiC mini-composite (b).

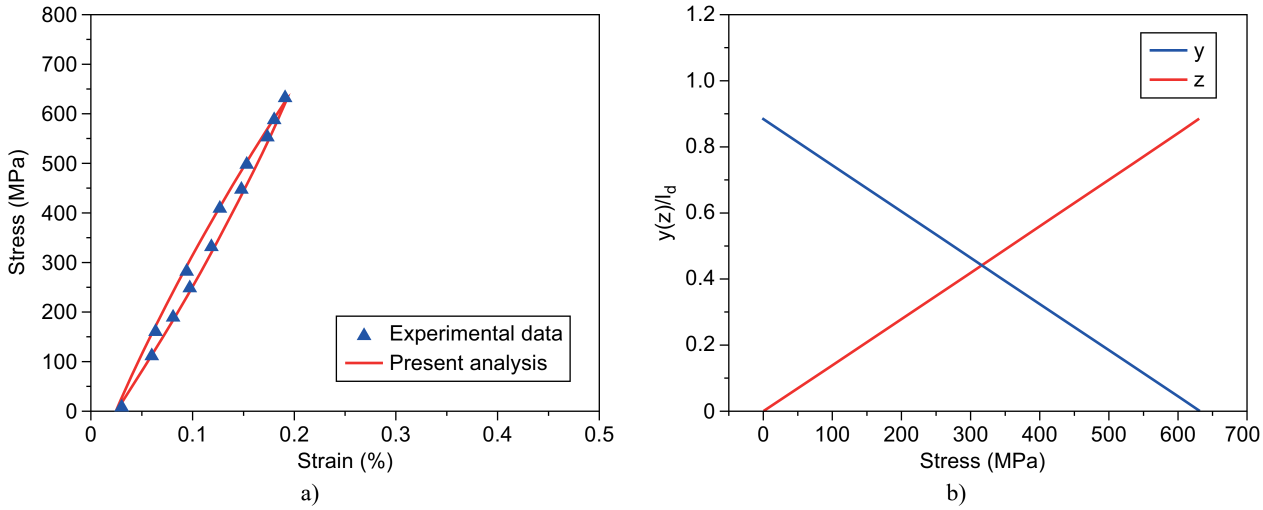

Figure 11. The experimental and predicted fatigue loading/unloading hysteresis loops (a) and the experimental and predicted interface slip length versus the applied stress curves of the Type B Hi-NicalonTM Type S SiC/SiC mini-composite under the peak stress of σ_{max} = 632 MPa (b).

is determined using Equation 2, and the fatigue loading/unloading hysteresis loop is predicted by Equations 7 and 8.

Tensile nonlinear strain and fatigue loading/unloading hysteresis loops of the Type C Hi-Nicalon^{TM} Type S SiC/SiC mini-composite

For the Type C Hi-Nicalon^{TM} Type S SiC/SiC mini-composite, the tensile stress-strain curve is predicted using the tensile constitutive model of Equation 4. The nonlinear tensile strain starts from the first matrix cracking stress of σ_{mc} =300 MPa, and the composite tensile strength is about σ_{UTS} = 860 MPa with the failure strain of ε_f = 0.62 %. The matrix cracking density is predicted using Equation 3 and increases from λ_{mc} = 0.02 mm^{-1} at σ_{mc} = 300 MPa to λ = 5.8/mm at σ_{sat} = 850 MPa, as shown in Figure 17 and Table 4. When the fatigue peak stress increases from σ_{max} = 485 MPa to σ_{max} = 743 MPa, the interface completely debonds and the fibre sliding

Table 4. The tensile nonlinear strain and fatigue loading/unloading hysteresis loops of the Type C Hi-NicalonTM Type S SiC/SiC mini-composite.

Tensile						
Items	σ_{mc} (MPa)	σ_{sat} (MPa)	σ_{UTS} (MPa)	ε_f (%)	λ_{mc} (mm^{-1})	λ_{sat} (mm^{-1})
Value	300	850	860	0.62	0.02	5.8

Fatigue					
Items	σ_{max} (MPa)	$2l_d/l_c$	$y(z)/l_d$	σ_{tr_fu} (MPa)	σ_{tr_fr} (MPa)
Value	485	1.0	0.824	–	–
	569	1.0	1.0	28.5	540.5
	662	1.0	1.0	264.8	397.2
	743	1.0	1.0	334.3	408.7

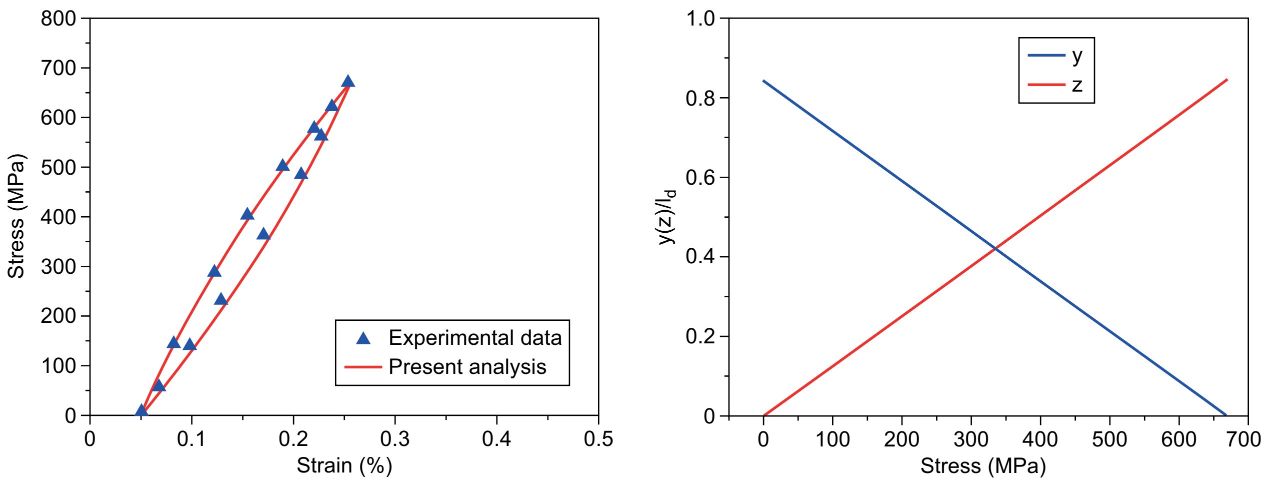

a) b)

Figure 12. The experimental and predicted fatigue loading/unloading hysteresis loops (a) and the experimental and predicted interface slip length versus the applied stress curves of the Type B Hi-NicalonTM Type S SiC/SiC mini-composite under the peak stress of σ_{max} = 669 MPa (b).

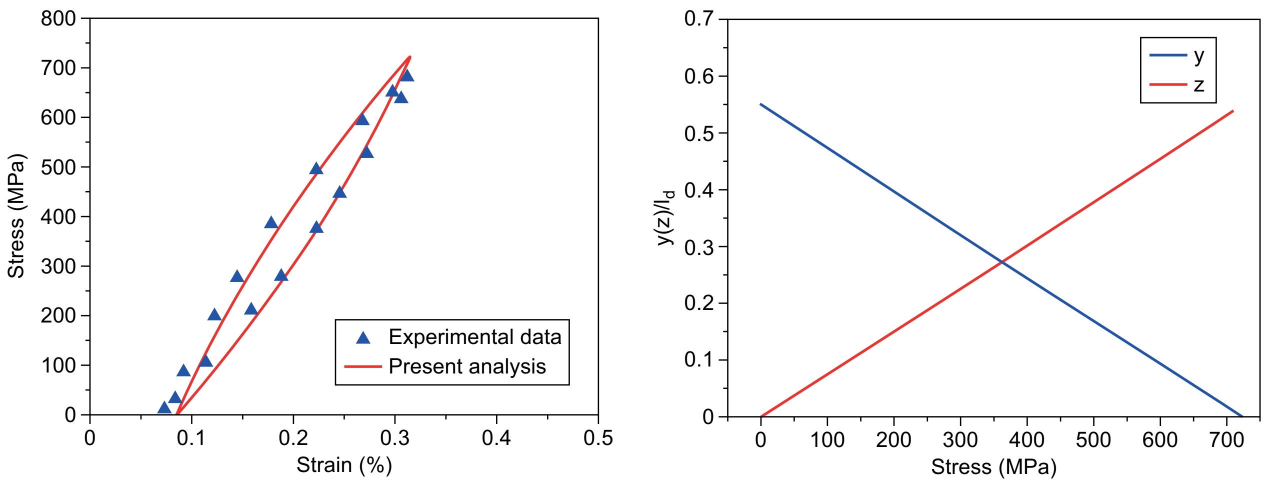

a) b)

Figure 13. The experimental and predicted fatigue loading/unloading hysteresis loops (a) and the experimental and predicted interface slip length versus the applied stress curves of the Type B Hi-NicalonTM Type S SiC/SiC mini-composite under the peak stress of σ_{max} = 724 MPa (b).

range increases from a partial slip (i.e., $y(z)/l_d < 1$) to a complete slip (i.e., $y(z)/l_d = 1$), and the interface debonding length is determined using Equation 2, and the fatigue loading/unloading hysteresis loop is predicted by Equations 5 and 6, as shown in Figures 18-21 and Table 4.

Tensile nonlinear strain and fatigue loading/unloading hysteresis loops of the Tyranno^{TM} SA3 SiC/SiC mini-composite

For the Tyranno^{TM} SA3 SiC/SiC mini-composite, the tensile nonlinear strain is predicted using the tensile constitutive model of Equation 4 and evolves from the first matrix cracking stress of σ_{mc} = 600 MPa to the saturation matrix cracking stress of σ_{sat} = 1000 MPa, and the corresponding matrix cracking density is predicted using Equation 3 and evolves from λ_{mc} = 1.6 mm^{-1} to λ_{sat} = 25 mm^{-1}, and the composite tensile strength is about σ_{UTS} = 1116 MPa with the failure strain of ε_f = 0.58 %, as shown in Figure 22 and Table 5. Under the peak

Table 5. The tensile nonlinear strain and fatigue loading/unloading hysteresis loops of the TyrannoTM SA3 SiC/SiC mini-composite.

Tensile						
Items	σ_{mc} (MPa)	σ_{sat} (MPa)	σ_{UTS} (MPa)	ε_f (%)	λ_{mc} (mm^{-1})	λ_{sat} (mm^{-1})
Value	600	1000	1116	0.58	1.6	25

Fatigue					
Items	σ_{max} (MPa)	$2l_d/l_c$	$y(z)/l_d$	σ_{tr_fu} (MPa)	σ_{tr_fr} (MPa)
Value	884	0.27	0.83	–	–
	933	0.45	0.78	–	–
	985	0.63	0.73	–	–

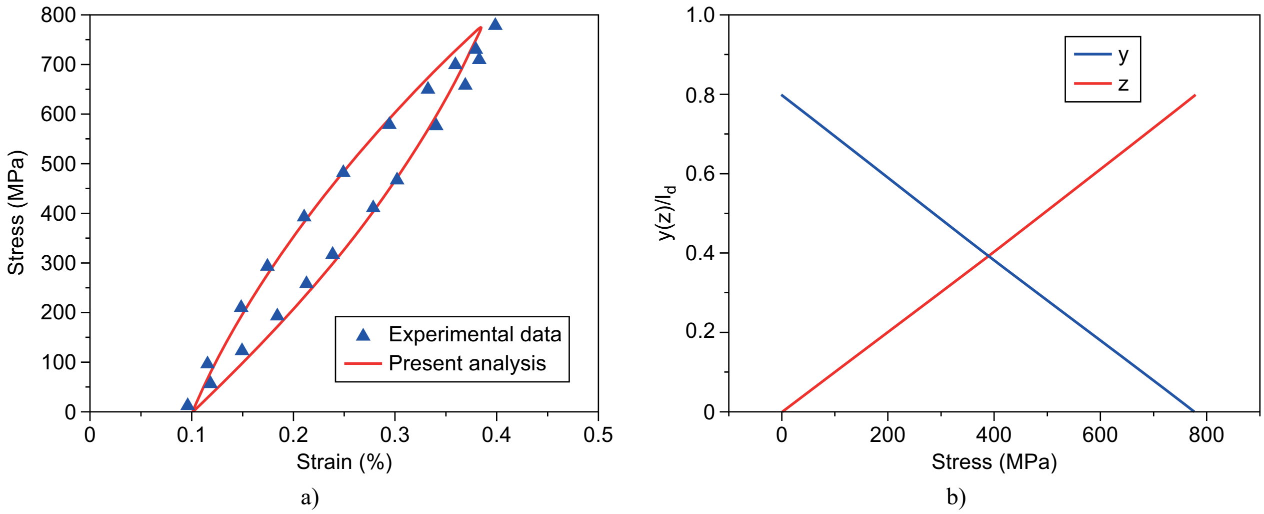

Figure 14. The experimental and predicted fatigue loading/unloading hysteresis loops (a) and the experimental and predicted interface slip length versus the applied stress curves of the Type B Hi-NicalonTM Type S SiC/SiC mini-composite under the peak stress of σ_{max} = 778 MPa (b).

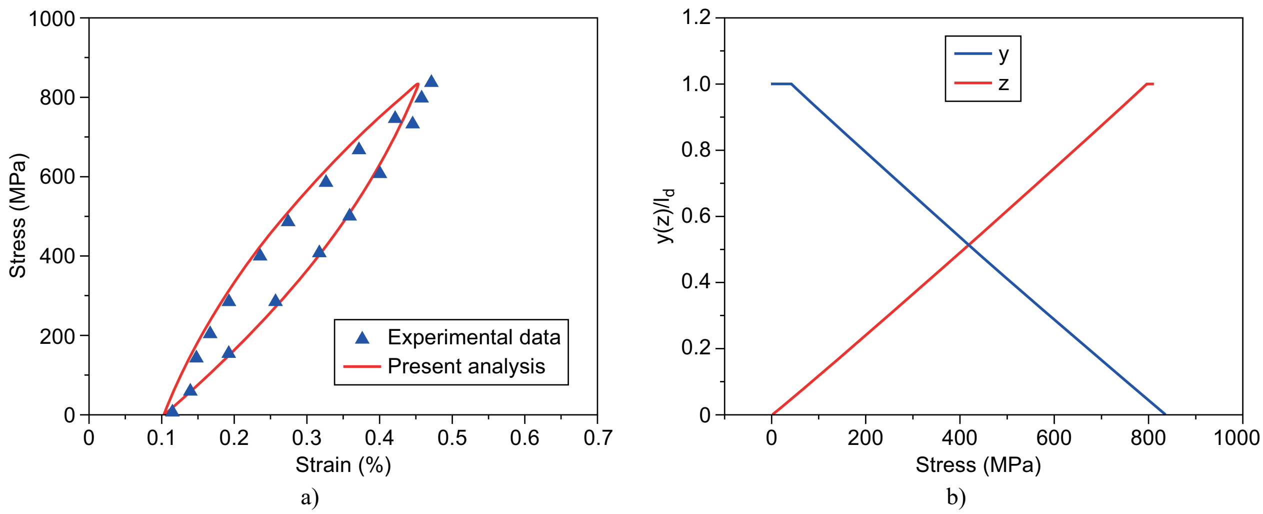

Figure 15. The experimental and predicted fatigue loading/unloading hysteresis loops (a) and the experimental and predicted interface slip length versus the applied stress curves of the Type B Hi-NicalonTM Type S SiC/SiC mini-composite under the peak stress of σ_{max} = 837 MPa (b).

stresses of σ_{max} = 884, 933, and 985 MPa, the interface debonds partially (i.e., $2l_d/l_c$ = 0.27, 0.45, and 0.63), and the fibre slides partially relative to the matrix (i.e., $y(z)/l_d$ = 0.83, 0.78, and 0.73), and the interface debonding length is determined using Equation 2, and the fatigue loading/unloading hysteresis loop is predicted by Equations 5 and 6, as shown in Figures 23-25 and Table 5.

CONCLUSION

In this paper, the tensile nonlinear strain and the fatigue loading/unloading hysteresis loops of the long-fibre-reinforced unidirectional mini-CMCs were investigated for different interface properties. The nonlinear tensile constitutive model and the fatigue loading/unloading constitutive model were developed considering different damage mechanisms. The relationships between the interface properties, tensile nonlinear strain, and fatigue loading/unloading hysteresis loops were established. The effects of the interface properties on the tensile damage and the fracture, fatigue loading/unloading hysteresis loops area, strain, and modulus were analysed. When the interface shear stress or interface debonding energy increases, the interface debonding length and slip length decrease, leading to a decrease in the tensile damage and failure strain, and the area, peak and residual strain of the fatigue loading/unloading hysteresis loops, and an increase in the fatigue hysteresis modulus. The tensile damage and fracture, and the fatigue loading/unloading hysteresis loops of the Hi-Nicalon™ and Tyranno™ SiC/SiC mini-composites with the different interface properties were analysed. The experimental matrix cracking evolution, tensile nonlinear strain, and fatigue loading/unloading hysteresis loops were predicted, and related to the interface debonding and slip condition.

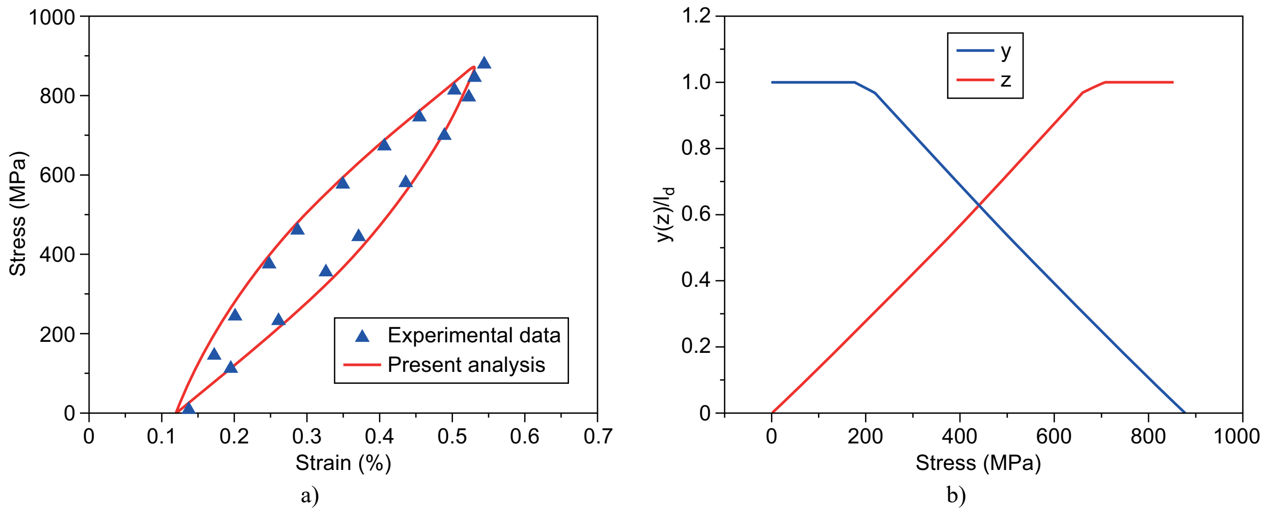

Figure 16. The experimental and predicted fatigue loading/unloading hysteresis loops (a) and the experimental and predicted interface slip length versus the applied stress curves of the Type B Hi-NicalonTM Type S SiC/SiC mini-composite under the peak stress of σ_{max} = 878 MPa (b).

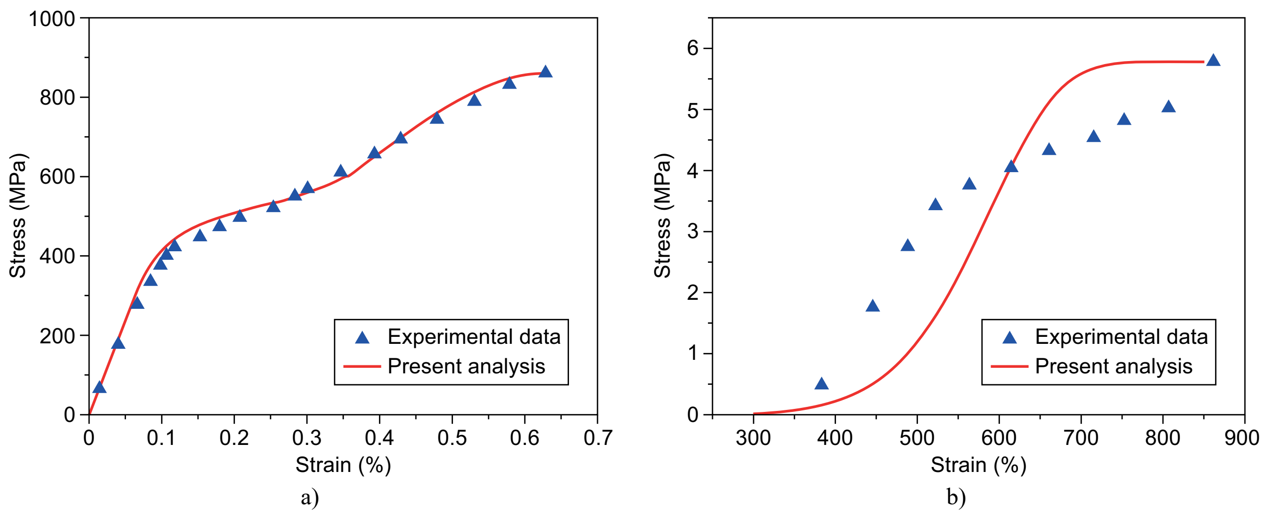

Figure 17. The experimental and predicted tensile stress-strain curves (a) and the experimental and predicted matrix cracking density versus the applied stress curves of the Type C Hi-NicalonTM Type S SiC/SiC mini-composite (b).

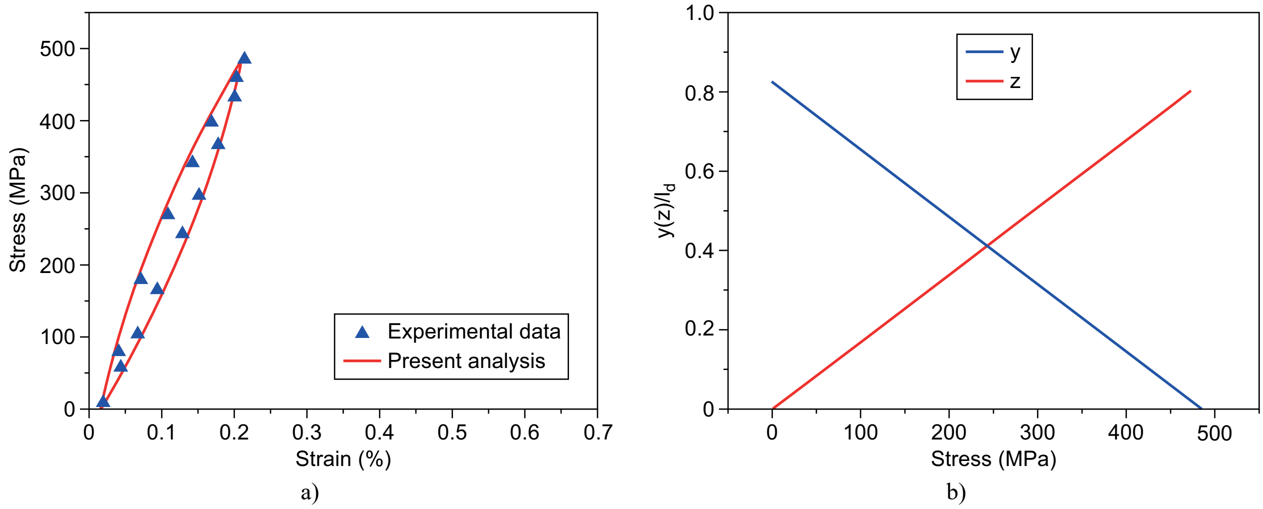

Figure 18. The experimental and predicted hysteresis loops (a) and the experimental and predicted interface slip lengths versus the applied stress curves of the Type C Hi-NicalonTM Type S SiC/SiC mini-composite under the peak stress of σ_{max} = 485 MPa (b).

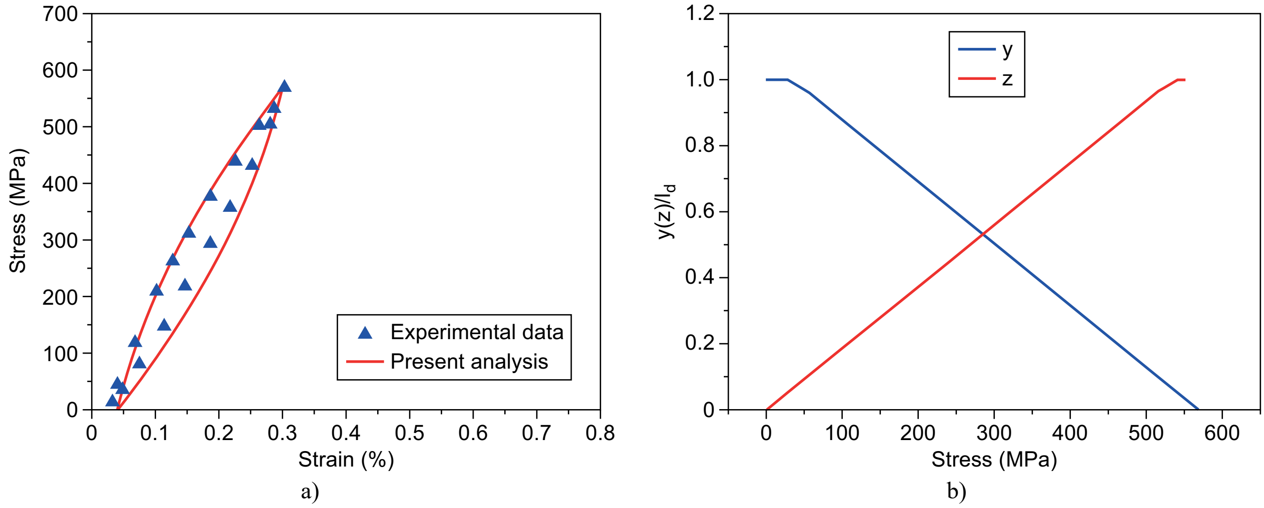

Figure 19. The experimental and predicted fatigue loading/unloading hysteresis loops (a) and the experimental and predicted interface slip length versus the applied stress curves of the Type C Hi-NicalonTM Type S SiC/SiC mini-composite under the peak stress of σ_{max} = 569 MPa (b).

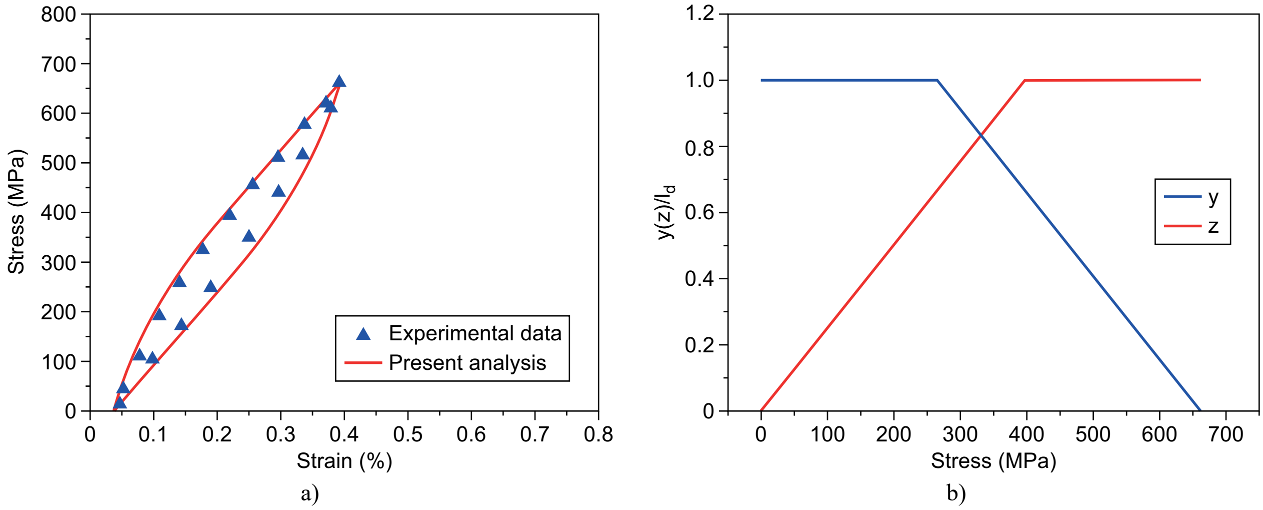

Figure 20. The experimental and predicted fatigue loading/unloading hysteresis loops (a) and the experimental and predicted interface slip length versus the applied stress curves of the Type C Hi-NicalonTM Type S SiC/SiC mini-composite under the peak stress of σ_{max} = 662 MPa (b).

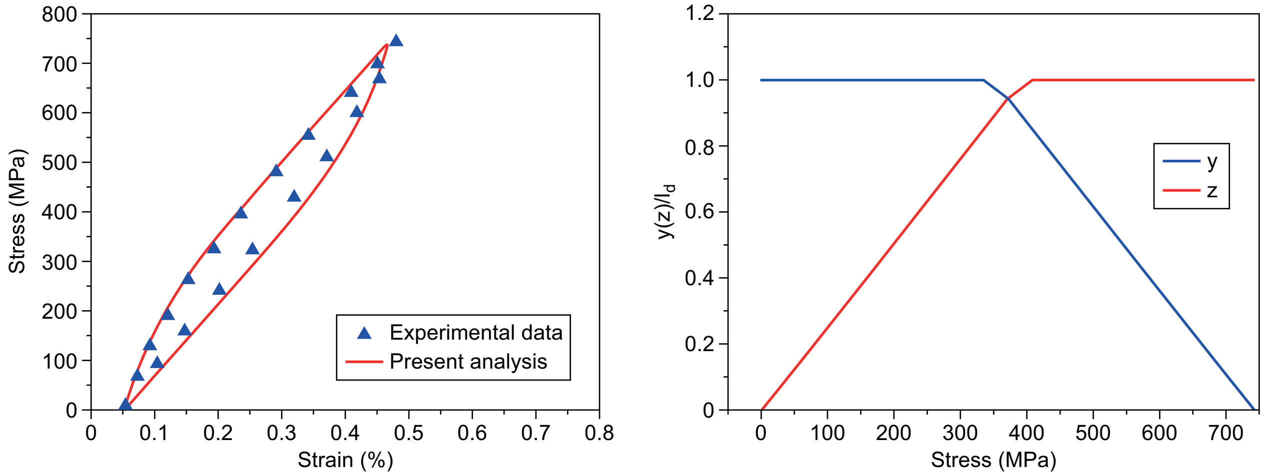

a) b)

Figure 21. The experimental and predicted fatigue loading/unloading hysteresis loops (a) and the experimental and predicted interface slip length versus the applied stress curves of the Type C Hi-NicalonTM Type S SiC/SiC mini-composite under the peak stress of σ_{max} = 743 MPa (b).

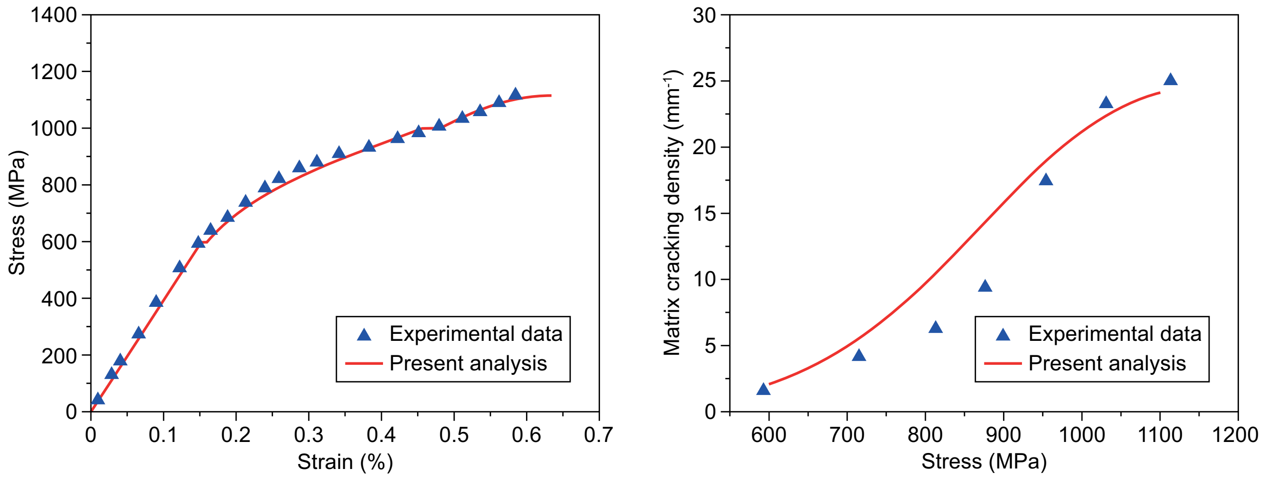

a) b)

Figure 22. The experimental and predicted tensile stress-strain curves (a) and the experimental and predicted matrix cracking density versus the applied stress curves of the TyrannoTM SA3 SiC/SiC mini-composite (b).

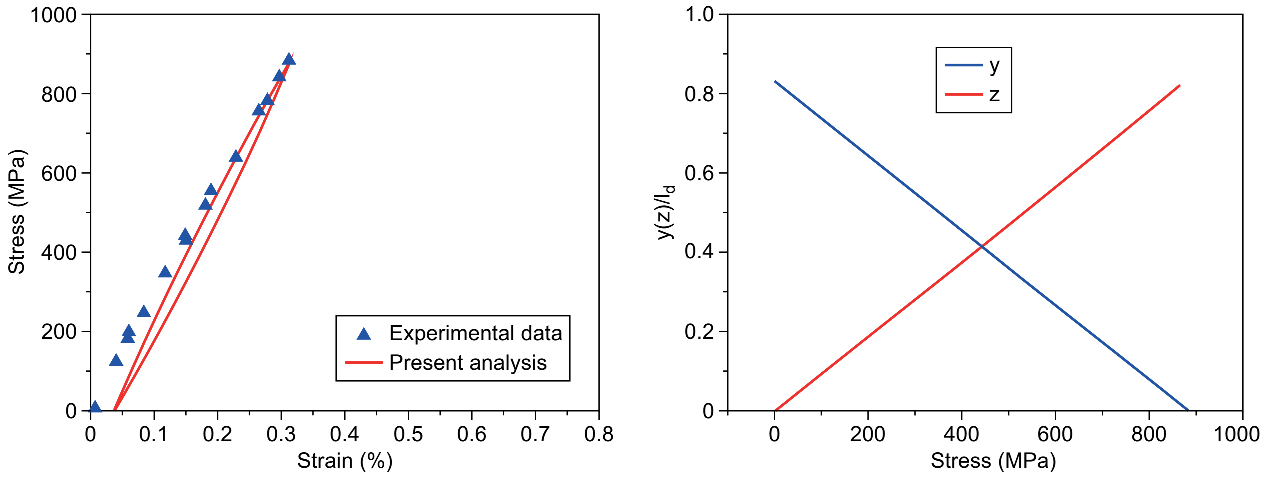

a) b)

Figure 23. The experimental and predicted fatigue loading/unloading hysteresis loops (a) and the experimental and predicted interface slip length versus the applied stress curves of the TyrannoTM SA3 SiC/SiC mini-composite under the peak stress of σ_{max} = 884 MPa (b).

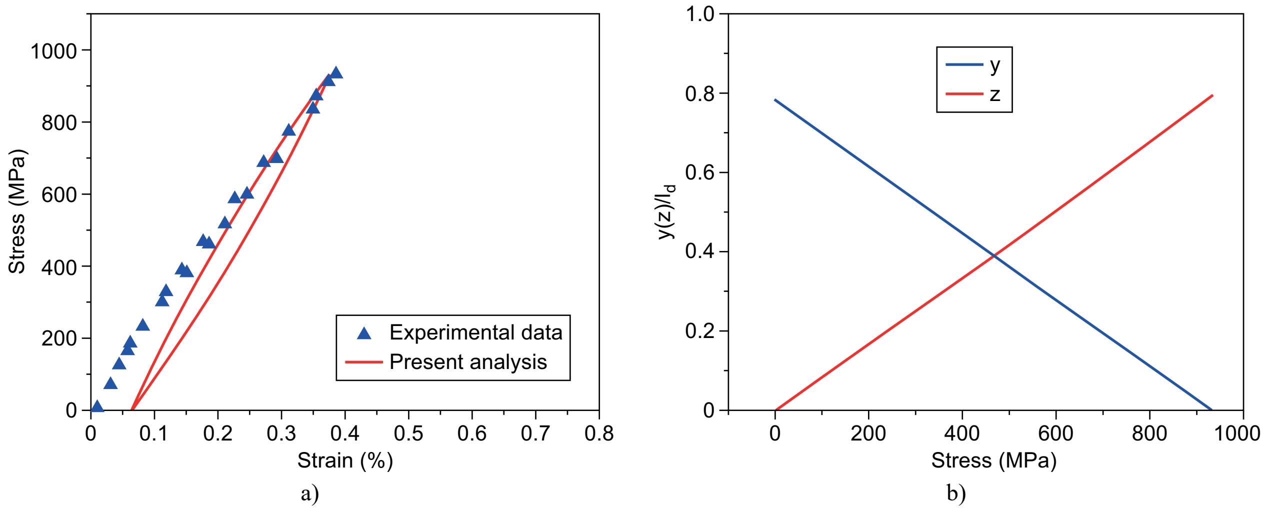

Figure 24. The experimental and predicted fatigue loading/unloading hysteresis loops (a) and the experimental and predicted interface slip length versus the applied stress curves of the TyrannoTM SA3 SiC/SiC mini-composite under the peak stress of σ_{max} = 933 MPa (b).

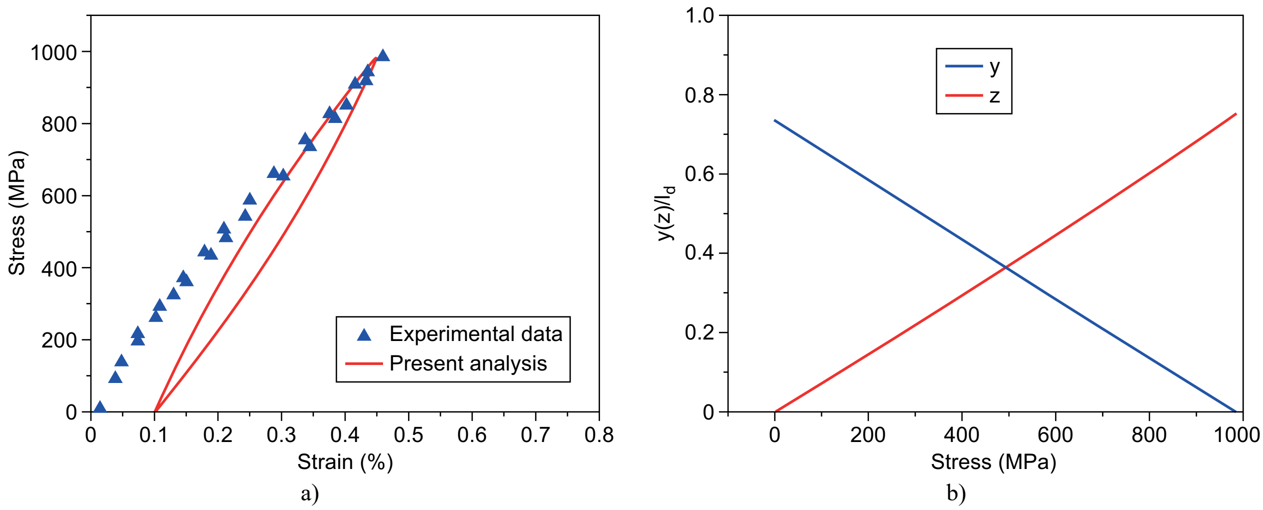

Figure 25. The experimental and predicted fatigue loading/unloading hysteresis loops (a) and the experimental and predicted interface slip length versus the applied stress curves of the TyrannoTM SA3 SiC/SiC mini-composite under the peak stress of σ_{max} = 985 MPa (b).

In the present analysis, there are significant differences between the modelling and experimental data of the matrix cracking density evolution curves. However, the experimental matrix cracking evolution is monitored using the the acoustic emission method, which may take the fibre/matrix interface debonding and the fibre failure signals of the matrix cracking into account, leading to the differences between the experimental and predicted results.

Acknowledgements

The work reported here is supported by the Fundamental Research Funds for the Central Universities (Grant No. NS2019038).

REFERENCES

1. Naslain R. (2004): Design, preparation and properties of non-oxide CMCs for application in engines and nuclear reactors: an overview. *Composites Science and Technology*, *64*(2), 155-170. doi: 10.1016/S0266-3538(03)00230-6
2. DiCarlo J. A., van Roode M. (2006). Ceramic composite development for gas turbine engine hot section components. In: *ASME Turbo Expo 2006: Power for Land, Sea, and Air* (pp. 221-231). American Society of Mechanical Engineers Digital Collection. doi: 10.1115/GT2006-90151
3. Li L. (2018). *Damage, fracture, and fatigue of ceramic-matrix composites*. Springer.
4. Li L. (2019). *Thermomechanical Fatigue of ceramic-matrix composites*. John Wiley & Sons. doi: 10.1002/9783527822614
5. Li L. (2019): Temperature-dependent proportional limit stress of carbon fiber-reinforced silicon carbide ceramic-

matrix composites. *Ceramics-Silikaty*, 63, 330–337. doi: 10.13168/cs.2019.0028

6. Li L. (2019): Time-dependent matrix multi-fracture of SiC/SiC ceramic-matrix composites considering interface oxidation. *Ceramics-Silikaty, 63*, 131–148. doi: 10.13168/cs.2019.0005
7. Naslain R. (1998): The design of the fiber-matrix interfacial zone in ceramic matrix composites. *Composites Part A: Applied Science and Manufacturing*, *29*(9-10), 1145-1155. doi: 10.1016/S1359-835X(97)00128-0
8. Rebillat, F. (2014). Advances in self-healing ceramic matrix composites. In: *Advances in Ceramic Matrix Composites*. Woodhead Publishing. pp. 475-514. doi: 10.1533/9780857098825.2.369
9. Yu H., Zhou X., Zhang W., Peng H., Zhang C. (2013): Mechanical behavior of SiCf/SiC composites with alternating PyC/SiC multilayer interphases. *Materials & Design*, *44*, 320-324. doi: 10.1016/j.matdes.2012.07.073
10. Xia Z., Li L. (2014). Understanding interfaces and mechanical properties of ceramic matrix composites. In: *Advances in Ceramic Matrix Composites.* Woodhead Publishing. pp. 267-285. doi: 10.1533/9780857098825.2.267
11. Li L., Xia Z. (2018). Role of interfaces in mechanical properties of ceramic matrix composites. In: Loe I.M. (Ed.) *Advances in Ceramic Matrix Composites*. Woodhead Publishing. doi: 10.1016/C2016-0-03477-0
12. Schonfeld K., Klemm H. (2019): Interaction of fiber matrix bonding in SiC/SiC ceramic matrix composites. *Journal of the European Ceramic Society, 39*(13), 3557-3565. doi: 10.1016/j.jeurceramsoc.2019.05.025
13. Li L. (2019): Modeling matrix multi-cracking evolution of fiber-reinforced ceramic-matrix composites considering fiber fracture. *Ceramics-Silikaty, 63*, 21-31. doi: 10.13168/cs.2018.0042
14. Zhu S., Mizuno M., Nagano Y., Kagawa Y., Kaya H. (1998): Tensile creep behavior of a SiC-fiber/SiC composite at elevated temperatures. *Composites Science and Technology, 57*, 1629−1637. doi: 10.1016/S0266-3538(97)00095-X
15. Li H., Morscher G. N., Lee J., Lee W. Y. (2004): Tensile and Stress-Rupture Behavior of SiC/SiC Minicomposite Containing Chemically Vapor Deposited Zirconia Interphase. *Journal of the American Ceramic Society*, *87*(9), 1726-1733. doi: 10.1111/j.1551-2916.2004.01726.x
16. Wang K., Chen L., Zheng X. (2010): Comparisons of tensile behavior of plain-woven carbon/silicon carbide composites at room temperature and high temperature. *Journal of Aeronautical Materials, 30,* 78−84.
17. Jing X., Yang X., Shi D., Niu H. (2017): Tensile creep behavior of three-dimensional four-step braided SiC/SiC composite at elevated temperature. *Ceramics International*, *43*, 6721−6729. doi: 10.1016/j.ceramint.2017.02.076
18. Li L. (2018): Modeling the monotonic and cyclic tensile stress-strain behavior of 2D and 2.5D woven C/SiC ceramic-matrix composites. *Mechanics of Composite Materials* , 54:165−178. doi: 10.1007/s11029-018-9729-5
19. Li L. (2019): A thermomechanical fatigue hysteresis-based damage evolution model for fiber-reinforced ceramic-matrix composites. *International Journal of Damage Mechanics*, *28*(3), 380-403. Doi: 10.1177/1056789518772162
20. Li L. (2019): Micromechanics modeling of fatigue hysteresis behavior in carbon fiber-reinforced ceramic-matrix composites. Part I: Theoretical analysis. *Composites Part B*, *159*, 502−513. doi: 10.1177/1056789518772162
21. Godin N., Reynaud P., Fantozzi G. (2019): Contribution of AE analysis in order to evaluate time to failure of ceramic matrix composites. *Engineering Fracture Mechanics*, *210*, 452−469. doi: 10.1016/j.engfracmech.2018.03.006
22. Wang Y., Zhang L., Cheng L., Ma J., Zhang W. (2008): Tensile performance and damage evolution of a 2.5-D C/SiC composite characterized by acoustic emission. *Applied Composite Materials*, *15*(4-6), 183-188. doi: 10.1007/s10443-008-9066-2
23. Evans A.G., Domergue J.M., Vagaggini E. (1994): Methodology for relating the tensile constitutive behavior of ceramic-matrix composites to constituent properties. *Journal of the American Ceramic Society*, *77*(6), 1425-1435. doi: 10.1111/j.1151-2916.1994.tb09739.x
24. Sorensen B.F., Holmes J.W. (1996): Effect of loading rate on the monotonic tensile behavior of a continuous-fiber-reinforced glass ceramic matrix composite. *Journal of the American Ceramic Society*, *79*, 313−320. doi: 10.1111/j.1151-2916.1996.tb08122.x
25. Ruggles-Wrenn M.B., Radzicki A.T., Baek S.S., Keller K.A. (2008): Effect of loading rate on the monotonic tensile behavior and tensile strength of an oxide-oxide ceramic composite at 1200ºC. *Materials Science and Engineering: A*, *492*(1-2), 88-94. doi: 10.1016/j.msea.2008.03.006
26. Mei H., Bai Q., Li H., Yu C., Cheng L. (2014): Effect of loading rate and temperature on monotonic tensile behavior in two-dimensional C/SiC composites. *Ceramics International, 40*, 16635−16640. doi: 10.1016/j.ceramint.2014.08.024
27. Zhu S., Gomyou T., Ochi Y., Ogasawara T. (2004): Effects of loading rate and temperature on tensile behavior of orthogonal three-dimensional woven Si–Ti–C–O fiber/Si-Ti–C–O matrix composites. *Journal of Materials Research*, *19*(10), 2964-2973. doi: 10.1557/JMR.2004.0375
28. Ahn B.K., Curtin W.A., Parthasarathy T.A., Dutton R.E. (1998): Criterion for crack deflection/penetration criterion for fiber-reinforced ceramic matrix composites. *Composites Science and Technology*, *58*(11), 1775-1784. doi: 10.1016/S0266-3538(98)00043-8
29. Carrere N., Martin E., Lamon J. (2000): The influence of the interphase and associated interfaces on the deflection of matrix cracks in ceramic matrix composites. *Composites Part A: Applied Science and Manufacturing*, *31*(11), 1179-1190. doi: 10.1016/S1359-835X(00)00095-6
30. Sauder C., Brusson A., Lamon J. (2010): Influence of interface characteristics on the mechanical properties of Hi-Nicalon type-S or Tyranno-SA3 fiber-reinforced SiC/SiC minicomposites. *International Journal Of Applied Ceramic Technology*, *7*(3), 291-303. doi: 10.1111/j.1744-7402.2010.02485.x
31. Yu H., Zhou X., Zhang W., Peng H., Zhang C. (2013): Influence of SiC coating thickness on mechanical properties of SiC/SiC composite. *Journal of Nuclear Materials*, *442*(1-3), 53-59. doi: 10.1016/j.jnucmat.2013.08.038
32. Kabel J., Yang Y., Balooch M., Howard C., Koyanagi T., Terrani K.A., Katoh Y., Hosemann P. (2017): Micro-mechanical evaluation of SiC-SiC composite interphase properties and debond mechanisms. *Composites Part B: Engineering*, *131*, 173-183. doi: 10.1016/j.compositesb.2017.07.035
33. Pryce A.W., Smith P.A. (1992): Behavior of unidirectional and crossply ceramic matrix composites under quasi-static tensile loading. *Journal of Materials Science*, *27*(10), 2695-2704. doi: 10.1007/BF00540692

34. Pryce A.W., Smith P.A. (1993): Matrix cracking in unidirectional ceramic matrix composites under quasi-static and cyclic loading. *Acta Metallurgica et Materialia*, *41*(4), 1269-1281. doi: 10.1016/0956-7151(93)90178-U
35. Chateau C., Gelebart L., Bornert M., Crepin J., Caldemaison D., Sauder C. (2014): Modeling of damage in unidirectional ceramic matrix composites and multi-scale experimental validation on third generation SiC/SiC minicomposites. *Journal of the Mechanics and Physics of Solids*, *63*, 298-319. doi: 10.1016/j.jmps.2013.09.001
36. Morscher G.N., Sing M., Kiser J.D., Freedman M., Bhatt R. (2007): Modeling stress-dependent matrix cracking and stress-strain behavior in 2D woven SiC fiber reinforced CVI SiC composites. *Composites Science and Technology*, *67*(6), 1009-1017. doi: 10.1016/j.compscitech.2006.06.007
37. Li L., Song Y., Sun Y. (2014): Modeling the tensile behavior of unidirectional C/SiC ceramic-matrix composites. *Mechanics of Composite Materials*, *49*(6), 659-672. doi: 10.1007/s11029-013-9382-y
38. Li L., Song Y., Sun Y. (2013): Modeling loading/unloading hysteresis behavior of unidirectional C/SiC ceramic matrix composites. *Applied Composite Materials*, *20*(4), 655-672. doi: 10.1007/s10443-012-9294-3
39. Li L. (2018): Modeling out-of-phase thermomechanical fatigue hysteresis of long fiber-reinforced ceramic-matrix composites subjected to different loading sequences. *Journal of the Ceramic Society of Japan*, *126*(5), 346-353. doi: 10.2109/jcersj2.17233
40. Li L. (2019): Damage and fracture of fiber-reinforced ceramic-matrix composites under thermal fatigue loading in oxidizing atmosphere. *Journal of the Ceramic Society of Japan*, 127, 67−80. doi: 10.2109/jcersj2.18107
41. Lamon J., Rebillat F., Evans A.G. (1995): Microcomposite test procedure for evaluating the interface properties of ceramic matrix composites. J *Journal of the American Ceramic Society*, *78*, 401−405. doi: 10.1111/j.1151-2916.1995.tb08814.x
42. Guillaumat L., Lamon J. (1996): Fracture statistics applied to modeling the non-linear stress-strain behavior in microcomposites: Influence of interfacial parameters. *International Journal of Fracture*, *82*(4), 297-316. doi: 10.1007/BF00013235
43. Morscher G.N., Martinez-Fernandez J., Purdy M.J. (1996): Determination of interfacial properties using a single-fiber microcomposite test. *Journal of the American Ceramic Society*, *79*, 1083−1091. doi: 10.1111/j.1151-2916.1996.tb08551.x
44. Cho C.D., Holmes J.W., Barber J.R. (1991): Estimation of interfacial shear in ceramic composites from frictional heating measurements. *Journal of the American Ceramic Society*, *74*, 2802−2808. doi: 10.1111/j.1151-2916.1991.tb06846.x
45. Holmes J.W., Cho C.D. (1992): Experimental observation of frictional heating in fiber-reinforced ceramics. *Journal of the American Ceramic Society*, *75*, 929−938. doi: 10.1111/j.1151-2916.1992.tb04162.x
46. Staehler J.M., Mall S., Zawada L.P. (2003): Frequency dependence of high-cycle fatigue behavior of CVI C/SiC at room temperature. *Composites Science and Technology*, *63*, 2121−2131. doi: 10.1016/S0266-3538(03)00190-8
47. Evans A.G., Zok F.W., McMeeking R.M. (1995): Fatigue of ceramic matrix composites. *Acta Metallurgica et Materialia*, *43*, 859−875. doi: 10.1016/0956-7151(94)00304-Z
48. Reynaud P. (1996): Cyclic fatigue of ceramic-matrix composites at ambient and elevated temperatures. *Composites Science and Technology*, *56*, 809−814. doi: 10.1016/0266-3538(96)00025-5
49. Zhu S., Mizuno M., Kagawa Y., Mutoh Y. (1999): Monotonic tension, fatigue and creep behavior of SiC-fiber-reinforced SiC-matrix composites: a review. *Composites Science and Technology*, *59*, 833−851. doi: 10.1016/S0266-3538(99)00014-7
50. Fantozzi G., Reynaud P. (2009): Mechanical hysteresis in ceramic matrix composites. *Materials Science and Engineering: A*, *521*, 18-23. doi: 10.1016/j.msea.2008.09.128
51. Ruggles-Wrenn M.B., Christensen D.T., Chamberlain A.L., Lane J.E., Cook T.S. (2011): Effect of frequency and environment on fatigue behavior of a CVI SiC/SiC ceramic matrix composite at 1200 ºC. *Composites Science and Technology*, *71*, 190−196. doi: 10.1016/j.compscitech.2010.11.008
52. Dassios K.G., Aggelis D.G., Kordatos E.Z., Matikas T.E. (2013): Cyclic loading of a SiC-fiber reinforced ceramic matrix composite reveals damage mechanisms and thermal residual stress state. *Composites Part A: Applied Science and Manufacturing*, *44*, 105-113. doi: 10.1016/j.compositesa.2012.06.011
53. Li L. (2019): Synergistic effects of frequency and temperature on fatigue hysteresis of cross-ply SiC/MAS composite under tension-tension loading. Ceramics-Silikáty, 63, 51-66. doi:10.13168/cs.2018.0045
54. Li L. (2018): Modeling in-phase thermomechanical fatigue hysteresis loops of fiber-reinforced ceramic-matrix composites. *Ceramics-Silikáty, 62*, 240−247. doi: 10.13168/cs.2018.0017
55. Morscher G.N., Baker C. (2014): Electrical resistance of SiC fiber reinforced SiC/Si matrix composites at room temperature during tensile testing. *International Journal of Applied Ceramic Technology*, *11*(2), 263-272. doi: 10.1111/ijac.12175
56. Han Z., Morscher G. N. (2015). Electrical resistance and acoustic emission during fatigue testing of SiC/SiC composites. In: *Mechanical Properties and Performance of Engineering Ceramics and Composites X.* doi: 10.1002/9781119211310.ch4
57. Budiansky B., Hutchinson J.W., Evans A.G. (1986): Matrix fracture in fiber-reinforced ceramics. *Journal of the Mechanics and Physics of Solids*, *34*(2), 167-189. doi: 10.1016/0022-5096(86)90035-9
58. Lissart N., Lamon J. (1997): Damage and failure in ceramic matrix minicomposites: Experimental study and model. *Acta Materialia*, *45*(3), 1025-1044. doi: 10.1016/S1359-6454(96)00224-8
59. Li L., Song Y. (2010): An approach to estimate interface shear stress of ceramic matrix composites from hysteresis loops. *Applied Composite Materials*, *17*(3), 309-328. doi: 10.1007/s10443-009-9122-6
60. Vagaggini E., Domergue J.-M., Evans A.G. (1995): Relationships between hysteresis measurements and the constituent properties of ceramic matrix composites: I Theory. *Journal of the American Ceramic Society*, *78*, 2709−2720. doi: 10.1111/j.1151-2916.1995.tb08046.x